Engineering Science and Technology, an International Journal 77 (2026) 102327

Contents lists available at ScienceDirect

Engineering Science and Technology, an International Journal

journal homepage: www.elsevier.com/locate/jestch

Full length article

# Benchmarking nonlinear controllers for a Quad Active Bridge resonant converter supplying pulsed power loads in DC microgrids

Aphrodis Nduwamungu [a,*,1], Tek Tjing Lie [a,2], Nirmal K.C. Nair [b,3], Ionis Lestas [c,4]

[a] Department of Electrical and Electronic Engineering, Auckland University of Technology, Auckland 1010, New Zealand
[b] Department of Electrical, Computer and Software Engineering, University of Auckland, Auckland 1010, New Zealand
[c] University of Cambridge, The Old Schools, Trinity Lane, Cambridge CB2 1TN, United Kingdom

ARTICLE INFO

*Keywords:*
Integral HOSM
Model predictive control with ISMC
ASSOSMC
OPAL-RT

ABSTRACT

This paper investigates advanced nonlinear control strategies for a Quad Active Bridge (QAB) resonant converter supplying pulsed power loads (PPLs) in DC microgrids, where fast load transients and inter-port coupling challenge voltage stability. Three controllers are designed and evaluated for regulating the 48 V ports 3 and 4 under a PPL step from 100 W to 200 W: ASSOSMC, IHOSMC, and CMPC–ISMC. In terms of voltage regulation, ASSOSMC achieves the smallest peak deviations ($\Delta V_3$ = 0.5 V, $\Delta V_4$ = 0.3 V), whereas IHOSMC and CMPC–ISMC exhibit larger voltage dips of 3.0/2.8 V and 3.5/4.2 V at ports 3/4, respectively. Overshoot is kept below 1.531% (ASSOSMC) and limited to 0.667% (IHOSMC and CMPC–ISMC), with fast settling times of 3.6 μs (ASSOSMC and CMPC–ISMC) and 4.7 μs (IHOSMC). Energy efficiency is evaluated from steady-state averaged port powers over a common interval ($t$ = 2.1166–2.8610 s): CMPC–ISMC achieves the highest overall efficiency ($\eta_{tot} \approx 90.775\%$), followed by ASSOSMC ($\eta_{tot} \approx 90.724\%$) and IHOSMC ($\eta_{tot} \approx 89.055\%$). Hardware-in-the-loop validation on an OPAL-RT platform confirms the effectiveness of the proposed controllers for stabilizing QAB port voltages under PPL disturbances, and highlights CMPC–ISMC as a balanced solution combining high efficiency with reduced current stress on the regulated ports.

## 1. Introduction

The growing adoption of DC microgrids (MGs) in critical applications such as data centeres, electric vehicles, and aerospace systems demands power converters that are not only highly efficient but also capable of maintaining stability under rapidly varying and nonlinear load conditions [1]. The Quad Active Bridge (QAB) converter emerges as a promising topology due to its modular structure, high-power density, and bidirectional power transfer capabilities [2,3]. However, when supplying pulsed power loads (PPLs) which introduce large, rapid transients that challenge voltage regulation, system stability and dynamic disturbances the control complexity and stability risks increase significantly [4,5].

Traditional linear controllers often struggle to deliver fast and robust regulations under highly dynamic conditions. Pulsed Power Loads (PPLs) are used in a range of specialized applications, including shipboard systems [6], Electromagnetic Aircraft Launchers(EAL), Electromagnetic Railguns (EMR), Free-Electron Lasers (FEL), high-energy lasers, radar systems, and medical equipment such as X-ray machines [7]. Intelligent DC microgrids can be viewed as cyber–physical energy systems because their coordination depends on communication networks, where delays (and packet loss and cyber-attacks) can degrade secondary control performance [8]. Secondary control aims to restore bus voltage and ensure proportional current sharing under these communication constraints, motivating fast local converter regulation that remains compatible with delayed, sampled coordination. Experimental validation is essential to capture timing and implementation effects and to confirm delay tolerance under realistic conditions.

To address the challenges posed by these rapidly varying loads, this research proposes several advanced control strategies that integrate disturbance observers with nonlinear sliding mode techniques. These approaches aim to enhance system robustness, minimize chattering, and maintain stable voltage regulation despite unpredictable load variations. The main objective of this work is to analyse the dynamic

* Corresponding author.
*E-mail addresses:* aphrodis.nduwamungu@autuni.ac.nz (A. Nduwamungu), tek.lie@aut.ac.nz (T.T. Lie), n.nair@auckland.ac.nz (N.K.C. Nair), icl20@cam.ac.uk (I. Lestas).
[1] PhD Candidate at Auckland University of Technology, New Zealand.
[2] Head of the School at Auckland University of Technology, New Zealand.
[3] Professor at the University of Auckland, New Zealand.
[4] Professor at the University of Cambridge, United Kingdom.

https://doi.org/10.1016/j.jestch.2026.102327
Received 2 November 2025; Received in revised form 10 January 2026; Accepted 26 February 2026
Available online 21 March 2026

performance and stability of three nonlinear controllers applied to QAB converters operating under PPLs.

The main contributions of this paper are as follows:

1. A novel *Adaptive Suboptimal Second-Order Sliding Mode Controller* (ASSOSMC) is developed for regulating QAB ports 3 and 4 under pulsed power load (PPL) disturbances, and is validated in both simulation and OPAL-RT real-time (OP5700 RCP/HIL) implementation.
2. An *Integral Higher-Order Sliding Mode Controller* (IHOSMC), as an established method, is implemented and adapted for the same QAB–PPL operating conditions to provide a rigorous benchmark, with performance verified in simulation and OPAL-RT HIL tests.
3. A *Combined Model Predictive Control with Integral Sliding Mode Control* (CMPC–ISMC), as an established strategy, is implemented and evaluated for the QAB–PPL system to compare robustness, dynamic performance, and energy-efficiency indicators against ASSOSMC, using both simulation and OPAL-RT HIL tests under identical scenarios.
4. A fair benchmarking framework is provided with unified test conditions (48 V regulation, a 100–200 W PPL step, and identical limits/constraints) and quantitative metrics (voltage deviation, overshoot, settling time, current stress, and efficiency/loss indicators) to ensure consistent comparison across the three controllers.

The paper is organized as follows: Section 1 presents the introduction. Section 2 discusses the modelling and operational principles of the QAB converter. Section 3 introduces and analyses the proposed control strategies. Section 4 presents simulation results and comparative analyses. Sections 4.4 and 4.5 detail the simulation and experimental results, respectively. Section 5 concludes the paper and offers recommendations for future work.

## 2. QAB converter topology and dynamic analysis

### 2.1. Topology of the QAB resonant converter with PPLs

This research investigates advanced control strategies and conducts a comprehensive stability analysis for the QAB network using a Single-Phase Shift (SPS) modulation scheme. The objective is to develop a control framework that ensures dynamic robustness, minimizes voltage deviations, and effectively handles transient energy demands from pulsed power loads in grid-connected DC MGs [9]. Fig. 1. depicts the architecture of the QAB converter which features a four-port structure comprising two input ports ($V_1$ and $V_2$) and two output ports($V_3$ and $V_4$). These ports are interconnected through a high-frequency transformer (HFT) with dual primary and dual secondary windings.

These PPLs impose sudden, high-magnitude current transients, introducing complex dynamic interactions between ports [9]. This configuration makes the QAB suitable for applications requiring isolated, high-efficiency power sharing between multiple ports but also demands advanced control to maintain voltage stability and minimize cross-port interference [10]. The QAB provides more flexibility in controlling energy transfer between numerous sources and loads than conventional topologies like DABs or LLC converters. This is important in DC MGs with dynamically fluctuating needs. Therefore, the QAB is a perfect type of converter topology for researching robust and predictive control strategies that can handle coupled port dynamics and maintain stability under light and strong transients, but this architectural advantage also adds more control complexity, especially under PPLs [7].

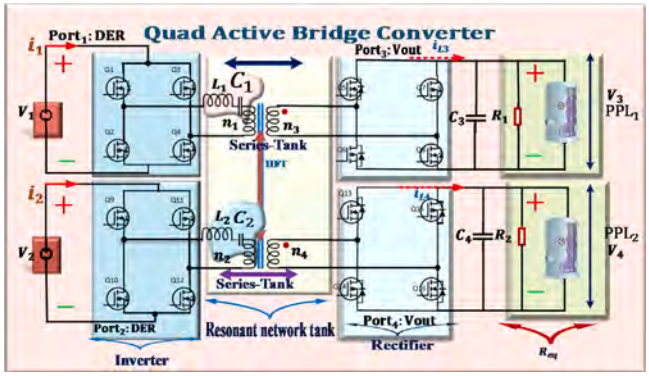


**Fig. 1.** QAB resonant converter supplying PPLs.

### 2.2. Comparative analysis of pulsed power converters

Table 2. presents a comprehensive qualitative overview of 22 research publications on QAB converter and pulsed power technologies. It highlights key aspects such as proposed converter architecture, control methods, application domains, performance metrics, and notable advancements or limitations. Fig. 2 summarises the 22 research publications on QAB converter systems and pulsed power technologies presented in Table 2.

Each row corresponds to a specific study, while the columns evaluate key performance parameters such as the number of switches, components, voltage stress, converter and control complexity, cost, efficiency, power density, input/output voltage range, weight, and stability. This structured overview serves as a valuable resource for critical analysis, helping to identify research trends and guide the selection of suitable converter designs for pulsed power and grid-connected applications [11].

Each parameter is rated on a scale from 1 to 5, where 5 indicates the best or most favourable performance, 1 the least favourable, and 0 denotes non-applicability(N/A). This systematic approach highlights the trade-offs and comparative advantages of different converter topologies, enabling consistent evaluation across studies. By visually representing strengths and limitations, the table supports informed decision-making and encourages the development of more efficient and reliable power conversion systems.

#### 2.2.1. QAB resonant tank and HFT model (reproducibility)

Fig. 1 depicts the implemented QAB resonant converter consisting of two identical power-transfer channels: Port 1↔Port 3 through the series resonant tank $(L_1, C_1)$ and Port 2↔Port 4 through $(L_2, C_2)$. In the simulation and HIL model, the resonant capacitors are implemented using the *Series RLC Branch* blocks (RC type) to include the capacitor equivalent series resistor (ESR) and the resonant inductors are implemented as series inductors. The high-frequency transformer (HFT) is implemented using the *Linear Transformer* block with a magnetizing branch $(R_m, L_m)$. The two channels use identical tank parameters ($L_2 = L_1$, $C_2 = C_1$), and the transformer turns ratio is defined by $n = V_1/V_2$ (here $n = 300/53 \approx 5.66$). The switching frequency is $f_{sw} = 14$ kHz and the OPAL-RT fixed-step execution (and discrete PWM update) is $T_s = 10$ µs, with a deadtime (gate delay) of $T_d = 0.25$ µs applied in the PWM gating path. All numerical values are summarized in Table 1.

#### 2.2.2. Impact of resonant-parameter mismatches

In practice, the resonant-tank parameters and transformer turns ratio may deviate from their nominal values due to component tolerances, temperature drift, and unmodelled parasitics. Such mismatches mainly

**Table 1**
QAB resonant tank and transformer parameters used in simulation/HIL.

| Parameter | Value |
|---|---|
| Switching frequency $f_{sw}$ | 14 kHz |
| Fixed-step/PWM update $T_s$ | $1\times10^{-5}$ s |
| Deadtime (gate delay) $T_d$ | $25\times10^{-8}$ s |
| Resonant inductors $L_1 = L_2$ | $100\times10^{-6}$ H |
| Resonant capacitors $C_1 = C_2$ | $1.29\times10^{-6}$ F |
| Capacitor ESR (Series RC branch) | $R_{C1} = R_{C2} = 10^{-4}$ Ω |
| Transformer nominal rating $(P_n, f_n)$ | (40 kVA, 14 kHz) |
| Primary winding $(V_1, R_1, L_{\sigma1})$ | (300 V, 43 mΩ, $15\times10^{-7}$ H) |
| Secondary winding $(V_2, R_2, L_{\sigma2})$ | (53 V, $2\times10^{-5}$ Ω, $15\times10^{-7}$ H) |
| Magnetizing branch $(R_m, L_m)$ | (40 kΩ, 5 mH) |
| Turns ratio $n = V_1/V_2$ | $300/53 \approx 5.66$ |

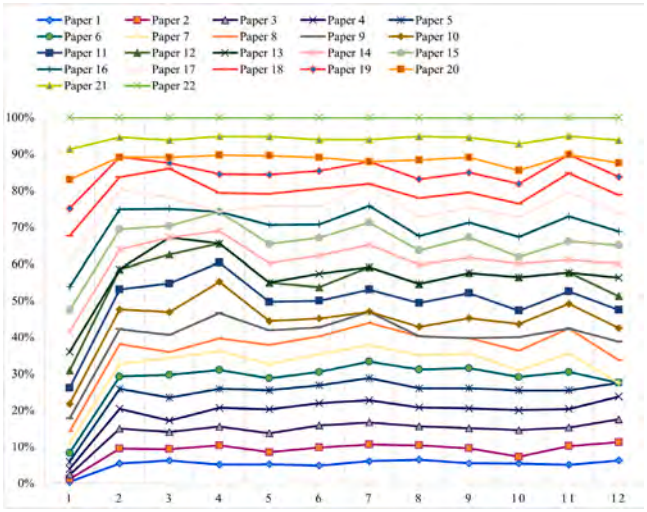


**Fig. 2.** Multicriteria analysis of pulsed power load converter topologies.

affect the phase-shift-to-tank-current (and phase-shift-to-power) mapping used by the predictive model and can be treated as a bounded uncertainty. Accordingly, the closed-loop sliding dynamics can be written as Eq. (1a):

$$\dot{S}_i(t) = -\varepsilon\ \mathrm{sat}\big(S_i(t)/\delta\big) - \gamma S_i(t) + d_i(t), \qquad |d_i(t)| \le \bar{d}_i,\quad i \in \{3,4\}, \tag{1a}$$

where $S_i(t)$ is the sliding (mismatch) variable for port $i \in \{3,4\}$, $\dot{S}_i(t)$ denotes its time derivative, $\varepsilon > 0$ is the nonlinear reaching gain, $\mathrm{sat}(\cdot)$ is the saturation function used to mitigate chattering, $\delta > 0$ is the boundary-layer thickness, $\gamma > 0$ is the linear damping gain, and $d_i(t)$ is a lumped disturbance term accounting for resonant-parameter errors and unmodelled dynamics, assumed bounded by $|d_i(t)| \le \bar{d}_i$ with $\bar{d}_i > 0$. Since the ISMC stability has already been established via a Lyapunov argument, the same conclusion holds under bounded mismatches by selecting the reaching gain $\varepsilon > \bar{d}_i$ (with $\delta$ setting the accuracy–chattering trade-off). Quantitatively, we evaluate ±20% variations in $(L_r, C_r)$ and ±5% in $n$ around the nominal values and report the resulting peak voltage deviation $\Delta V_{\max}$ (and settling time) at Ports 3 and 4, confirming robust regulation with bounded transients under the tested mismatch levels.

## 3. Control strategies and stability analysis for a QAB converter

The QAB converter supplying PPLs experiences sharp transients, voltage fluctuations, and complex inter-port interactions, exposing significant control challenges despite its effectiveness for multi-port transfer. Conventional controllers such as proportional integral (PI), sliding mode control (SMC), super twisting sliding mode control(STSMC), struggle to maintain stability under these fast dynamics [33]. Meeting requirements for fast voltage regulation, inter-port coupling mitigation, soft-switching, and robustness to uncertainties/disturbances is essential [34]. Hence the move to advanced nonlinear/predictive strategies CMPC with ISMC, ASSOSMC, and IHOSMC with CMPC with ISMC specifically targeting nonlinear, time-varying PPL disturbances [35]. Although conservative, MPC enforces limits and offers optimal finite-horizon forecasts [35]. ISMC achieves robustness, zero steady-state error, and quick disturbance rejection using an integral sliding manifold and nonlinear corrective action [36]. The hybrid CMPC-ISMC combines these strengths to handle PPL-induced dynamics while retaining excellent tracking. The models target a QAB converter with loads on Port 1↔Port 3 and Port 2↔Port 4, starting with the capacitor-voltage dynamics at ports 3 and 4 Eq. (1) (see Fig. 1).

$$\begin{cases} C_3 \dfrac{dv_{c_3}(t)}{dt} = i_{L_3}(t) - \left( \dfrac{v_{c_3}(t)}{R_{\mathrm{load},3}} + \dfrac{P_{\mathrm{PPL},3}}{v_{c_3}(t)} \right), \\ C_4 \dfrac{dv_{c_4}(t)}{dt} = i_{L_4}(t) - \left( \dfrac{v_{c_4}(t)}{R_{\mathrm{load},4}} + \dfrac{P_{\mathrm{PPL},4}}{v_{c_4}(t)} \right) \end{cases} \tag{1}$$

where $v_{c_i}(t)$ is the capacitor voltage; $i_{L_i}(t)$ is the control input from converter switching; $\frac{v_{c_i}(t)}{R_{\mathrm{load},i}}$ is the resistive-load current; $\frac{P_{\mathrm{PPL},i}}{v_{c_i}(t)}$ is the PPL equivalent current; and $C_i$ is the port capacitance ($i \in \{3,4\}$).

### 3.0.1. Pulsed -load characterization

To improve reproducibility and reflect realistic pulsed-load behaviour, the pulsed power load (PPL) at Ports 3 and 4 is modelled as a time-varying constant-power load, $i_{\mathrm{PPL},i}(t) = P_{\mathrm{PPL},i}(t)/v_{c_i}(t)$, $i \in \{3,4\}$. Instead of an ideal instantaneous square pulse, $P_{\mathrm{PPL},i}(t)$ is implemented as a trapezoidal periodic pulse with finite rise and fall times to emulate practical pulse generation and conversion limits. The pulse profile is fully defined by the baseline power $P_{\min}$, pulse magnitude $P_\Delta$, rise time $t_r$, flat-top duration $t_{\mathrm{on}}$, fall time $t_f$, and period $T$; the pulse energy is $E_{\mathrm{pulse}} = P_\Delta\left(t_{\mathrm{on}} + \frac{t_r+t_f}{2}\right)$.

In addition, a staircase excitation (100–200 W increments) is applied to represent multi-level pulsed loads. All pulse parameters ($P_{\min}$, $P_\Delta, t_r, t_{\mathrm{on}}, t_f, T$) are reported to ensure repeatability. The tracking error for ports 3 and 4 is defined in Eq. (2).

$$\begin{cases} e_3(t) = v_{\mathrm{ref},3}(t) - v_{c_3}(t), \\ e_4(t) = v_{\mathrm{ref},4}(t) - v_{c_4}(t) \end{cases} \tag{2}$$

where, $v_{\mathrm{ref},3} = v_{\mathrm{ref},4} = 48$ V is the reference voltage for ports 3 and 4.

Let us define the integral sliding manifolds( $s_i(t)$ ) for ports 3 and 4 as Eq. (3) .

$$\begin{cases} S_3(t) = e_3(t) + \lambda_3 \displaystyle\int_0^t e_3(\tau)\, d\tau \\ S_4(t) = e_4(t) + \lambda_4 \displaystyle\int_0^t e_4(\tau)\, d\tau \end{cases} \tag{3}$$

where, ( $s_i(t)$ ) is sliding surface combining error and integral, $\lambda_i > 0$ is the integral weight to improve steady-state tracking. Compute sliding surface derivative for an Eq. (4).

$$\begin{cases} \dot{S}_3(t) = \dot{e}_3(t) + \lambda_3\, e_3(t) \\ \dot{S}_4(t) = \dot{e}_4(t) + \lambda_4\, e_4(t) \end{cases} \tag{4}$$

consequently, from Eqs. (1)–(2), substitute $\dfrac{dv_{c_i}(t)}{dt}$ for ports 3 and 4 and determine the derivative of the sliding mode which is given by Eq. (5):

$$\begin{cases} \dot{S}_3(t) = \dot{v}_{\mathrm{ref},3}(t) - \dfrac{1}{C_3}\left( i_{L_3}(t) - \dfrac{v_{c_3}(t)}{R_{\mathrm{load},3}} - \dfrac{P_{\mathrm{PPL},3}}{v_{c_3}(t)} \right) + \lambda_3\big(v_{\mathrm{ref},3}(t) - v_{c_3}(t)\big) \\ \dot{S}_4(t) = \dot{v}_{\mathrm{ref},4}(t) - \dfrac{1}{C_4}\left( i_{L_4}(t) - \dfrac{v_{c_4}(t)}{R_{\mathrm{load},4}} - \dfrac{P_{\mathrm{PPL},4}}{v_{c_4}(t)} \right) + \lambda_4\big(v_{\mathrm{ref},4}(t) - v_{c_4}(t)\big) \end{cases} \tag{5}$$

**Table 2**
Comparative analysis of QAB converters supplying pulsed power loads.

| No | Ref | Components | Switches | Voltage stress | Converter complexity | Control complexity | Cost | Efficiency | Power density | Input/Output voltage range | Weight | Stability |
|---|---|---|---|---|---|---|---|---|---|---|---|---|
| 1 | [10] | High | 8+ | Reduced | High | High | High | Very high | High | 700–800 V/250–500 V | Moderate | Excellent |
| 2 | [12] | Medium | 6+ | Moderate | Moderate | High | Med. | Good | Medium | 100 V | Reduced | Improved |
| 3 | [13] | High | Multiple | Moderate | High | Very high | High | High | High | 500–900 V/270–750 V | Moderate | Very high |
| 4 | [14] | High | Multiple | Moderate | Very high | Very high | High | High | High | 400–800 V/400–48 V | Moderate | Excellent |
| 5 | [15] | High | 12+ | Moderate | High | High | High | High | High | 400–800 V | Medium | Good |
| 6 | [16] | Medium | 6+ | Reduced | Moderate | Moderate | Med. | High | Improved | 300 V/28–100 V | Reduced | Stable |
| 7 | [17] | Medium | 4+ | Moderate | Moderate | High | Med. | Good | Moderate | 28 V | Moderate | Stable |
| 8 | [18] | High | Multiple | Low | High | High | High | Good | High | 300–800 V/28–72 V | High | Very high |
| 9 | [19] | Moderate | N/A | Variable | Moderate | Low | Low | N/A | N/A | 400 V/50–400 V | N/A | High |
| 10 | [20] | High | Few | Very high | Low | Low | Low–Med. | Low | High | 380–600 V, 280–450 V | High | Moderate |
| 11 | [21] | High | 16+ | Moderate | High | High | High | Very high | Very high | 150–450 V/300–800 V | Low | High |
| 12 | [22] | High | 16+ | Medium | High | Moderate | High | High | High | 2–4 kV/400–1000 V | Moderate | Good |
| 13 | [23] | Model | Varies | Varies | N/A | Moderate | N/A | N/A | N/A | N/A | N/A | High |
| 14 | [24] | High | 8+ | Low | High | High | High | High | Compact | 380–400 V/48–72 V | Low | Good |
| 15 | [25] | High | Multiple | Moderate | High | High | Good | Good | High | 48–200 V | Reduced | High |
| 16 | [26] | High | 8+ | Moderate–High | High | Moderate | Med. | Good | Moderate | 600–800 V/200–500 V | High | Good |
| 17 | [27] | High | Multiple | Controlled | High | High | High | High | Moderate | 600 V | High | High |
| 18 | [28] | Medium | 8 | Moderate | Moderate | High | Med.–High | High | Moderate | 300 V/300 V | Moderate | High |
| 19 | [29] | High | 6+ | Reduced | High | High | High | High | High | 400–750 V/48–300 V | Reduced | High |
| 20 | [30] | Model | Varies | Configurable | High | Medium | N/A | Optimized | Topology-based | 100–800 V/48–500 V | N/A | Design-based |
| 21 | [31] | High | 8+ | Reduced | High | High | High | Very high | High | 700–800 V/250–500 V | Moderate | Excellent |
| 22 | [32] | High | Multiple | Moderate | High | Very high | High | High | High | 600–800 V/48–300 V | Moderate | Very high |

#### 3.0.2. Chattering mitigation with saturation function (sat)

The main objective of ISMC is to lead the sliding mode control to zero, and its equations are written as follows:

$$\begin{cases} \dot{S}_3(t) = -\varepsilon\ \mathrm{sat}\left(\dfrac{S_3(t)}{\delta}\right) - \gamma\, S_3(t) \\ \dot{S}_4(t) = -\varepsilon\ \mathrm{sat}\left(\dfrac{S_4(t)}{\delta}\right) - \gamma\, S_4(t) \end{cases} \tag{6}$$

where, $\varepsilon, \gamma > 0$ are the gains controlling convergence, $\delta > 0$ is the boundary layer for saturation, $\mathrm{sat}\left(\frac{S_i(t)}{\delta}\right)$ the saturation function, and defined as:

$$\mathrm{sat}\left(\frac{S_i(t)}{\delta}\right) = \begin{cases} +1, & \dfrac{S_i(t)}{\delta} > 1, \\ \dfrac{S_i(t)}{\delta}, & |S_i(t)| \le \delta, \\ -1, & \dfrac{S_i(t)}{\delta} < -1, \end{cases} \tag{7}$$

as a result, the sliding mode reaching law with chattering mitigation is enforced by setting Eq. (5) is equal to Eq. (6), as described by Eq. (8).

$$\begin{aligned} \dot{S}_i(t) &= \dot{v}_{\mathrm{ref},i}(t) - \frac{1}{C_i}\left(i_{L_i}(t) - \frac{v_{c_i}(t)}{R_{\mathrm{load},i}} - \frac{P_{\mathrm{PPL},i}}{v_{c_i}(t)}\right) + \lambda_i\big(v_{\mathrm{ref},i}(t) - v_{c_i}(t)\big) \\ &= -\varepsilon\ \mathrm{sat}\big(S_i(t)/\delta\big)\ -\ \gamma\, S_i(t). \end{aligned} \tag{8}$$

where $i \in \{3,4\}$ for ports 3 and 4. Then rearrange Eq. (8) to solve for the required current $i_{L_i}(t)$ defined by Eq. (9).

$$\begin{aligned} i_{L_i}(t) = C_i \Bigg[ & \dot{v}_{\mathrm{ref},i}(t) + \lambda_i\, e_i(t) + \frac{1}{C_i}\left(\frac{v_{c_i}(t)}{R_{\mathrm{load},i}} + \frac{P_{\mathrm{PPL},i}}{v_{c_i}(t)}\right) \\ & + \varepsilon\ \mathrm{sat}\big(S_i(t)/\delta\big) + \gamma\, S_i(t) \Bigg] \end{aligned} \tag{9}$$

now, assume state feedback is available, and proportional-integral feedback is used in place of $\dot{v}_{\mathrm{ref},i}(t)$ to generate the control input $u_{\mathrm{ISMC},i}(t)$. Let us consider that $u_{\mathrm{ISMC},i}(t) = i_{L_i}(t)$ so the ISMC final control law for ports 3 and 4 can be expressed by Eq. (10).

$$\begin{aligned} u_{\mathrm{ISMC},i}(t) = {} & k_i\left(v_{\mathrm{ref},i}(t) - v_{c_i}(t) + \lambda_i \int_0^t \big(v_{\mathrm{ref},i}(\tau) - v_{c_i}(\tau)\big)\, d\tau\right) \\ & + \left(\frac{v_{c_i}(t)}{R_{\mathrm{load},i}} + \frac{P_{\mathrm{PPL},i}}{v_{c_i}(t)}\right) \\ & + c_i\, \varepsilon\ \mathrm{sat}\left(\frac{v_{\mathrm{ref},i}(t) - v_{c_i}(t) + \lambda_i \int_0^t \big(v_{\mathrm{ref},i}(\tau) - v_{c_i}(\tau)\big)\, d\tau}{\delta}\right) \\ & + \frac{v_{\mathrm{ref},i}(t) - v_{c_i}(t) + \lambda_i \int_0^t \big(v_{\mathrm{ref},i}(\tau) - v_{c_i}(\tau)\big)\, d\tau}{\delta} + c_i\, \gamma\, S_i(t). \end{aligned} \tag{10}$$

where $k_i > 0$ is the manifold gain, $R_{\mathrm{load},i}$ is the resistive load, $P_{\mathrm{PPL},i}$ is the pulsed-load power modelled as a constant-power term, $c_i$ is a known scaling coefficient, $\varepsilon > 0$ is the reaching gain,where $i \in \{3,4\}$, $\delta > 0$ is the boundary-layer thickness, and $\gamma > 0$ is the linear damping gain. The function $\mathrm{sat}(\cdot)$ is employed to mitigate chattering.

#### 3.0.3. Stability analysis of the ISMC

Consider the Lyapunov function $V_i(t) = \frac{1}{2} S_i^2(t)$ for $i \in \{3,4\}$. Using the reaching law in Eq. (6),

$$\dot{V}_i(t) = S_i(t)\dot{S}_i(t) = -\varepsilon\, S_i(t)\, \mathrm{sat}\left(\tfrac{S_i(t)}{\delta}\right) - \gamma\, S_i^2(t) \le 0. \tag{10a}$$

Moreover, for $|S_i(t)| \ge \delta$, $\mathrm{sat}(S_i/\delta) = \mathrm{sign}(S_i)$ and hence $\dot{V}_i \le -\varepsilon|S_i| - \gamma S_i^2 < 0$, which guarantees finite-time reaching to the boundary layer $|S_i(t)| \le \delta$. Inside $|S_i(t)| \le \delta$, $\mathrm{sat}(S_i/\delta) = S_i/\delta$ and $\dot{S}_i = -(\varepsilon/\delta + \gamma)S_i$, implying exponential convergence of $S_i(t)$ to zero (practical convergence with boundary layer). Therefore, the ISMC ensures bounded closed-loop signals and robust voltage regulation under PPL disturbances.

where $i \in \{3,4\}$ denotes ports 3 and 4; $k_i\, e_i(t)$ is the proportional tracking action; $\lambda_i \int_0^t e_i(\tau)\, d\tau$ is the integral action ensuring zero steady-state error; $\lambda_i$ is the integral gain; and $k_i$ is the proportional gain. Integral Sliding Mode Control (ISMC) is highly robust to uncertainties and PPL-induced disturbances. On its own, however, ISMC cannot optimize performance while enforcing operational constraints. Integrating Model Predictive Control (MPC) supplies optimal, constraint-aware control. Although MPC's disturbance rejection is slower, the resulting hierarchical CMPC with ISMC scheme combines MPC's constraint handling with ISMC's rapid robustness [36].

#### 3.0.4. Mathematical equation for Model Predictive Control (MPC)

We linearize and discretize the QAB port dynamics (see Fig. 1) about a nominal operating point for Ports 3 and 4. The steady-state (operating-point) variables used for linearization are collected as follows:

$$\begin{cases} v_{c_3}^*,\ i_{L_3}^*,\ \Delta\varphi_3^* \\ v_{c_4}^*,\ i_{L_4}^*,\ \Delta\varphi_4^* \end{cases} \tag{11}$$

the corresponding small-signal perturbations about the operating point are defined as

$$\begin{cases} \overline{v}_{c_3}(t) = v_{c_3}(t) - v^*_{c_3} \\ \overline{v}_{c_4}(t) = v_{c_4}(t) - v^*_{c_4} \end{cases} \tag{12}$$

$$\begin{cases} \overline{i}_{L_3}(t) = i_{L_3}(t) - i^*_{L_3} \\ \overline{i}_{L_4}(t) = i_{L_4}(t) - i^*_{L_4} \end{cases} \tag{13}$$

$$\begin{cases} \overline{\Delta\varphi}_3(t) = \Delta\varphi_3(t) - \Delta\varphi^*_3 \\ \overline{\Delta\varphi}_4(t) = \Delta\varphi_4(t) - \Delta\varphi^*_4 \end{cases} \tag{14}$$

where $(\cdot)^*$ denotes the nominal value at the operating point, $v^*_{c_i}$ is the steady-state capacitor voltage (V), $i^*_{L_i}$ is the steady-state port inductor current (A), and $\Delta\varphi^*_i$ is the steady-state phase-shift command (rad), for $i \in \{3,4\}$. Here, $\Delta\varphi_i(t)$ denotes the commanded phase shift between the reference/input bridge and the bridge associated with port $i$, and $t$ denotes time (s).

*(a) Linearized load-port capacitor dynamics (including PPL).* At each load port, the total load current is modelled as a parallel combination of a resistive load and a power pulsed load: $i_{\text{load},i}(t) = v_{c_i}(t)/R_{\text{load},i} + P_i(t)/v_{c_i}(t)$, where $P_i(t)$ represents the (time-varying) PPL power level. Linearizing $i_{\text{load},i}$ about $(v^*_{c_i}, P^*_i)$ yields

$$\overline{i}_{\text{load},i}(t) = \left( \frac{1}{R_{\text{load},i}} - \frac{P^*_i}{(v^*_{c_i})^2} \right) \overline{v}_{c_i}(t) + \frac{1}{v^*_{c_i}} \overline{P}_i(t), \qquad i \in \{3,4\}, \tag{15}$$

where $\overline{P}_i(t) = P_i(t) - P^*_i$ is treated as an exogenous disturbance due to the PPL steps. Substituting (15) into the capacitor KCL $C_i \dot{v}_{c_i} = i_{L_i} - i_{\text{load},i}$ gives the linearized capacitor-voltage dynamics:

$$C_i \frac{d\,\overline{v}_{c_i}(t)}{dt} = \overline{i}_{L_i}(t) - G_i\,\overline{v}_{c_i}(t) - \frac{1}{v^*_{c_i}} \overline{P}_i(t), \qquad i \in \{3,4\}, \tag{16}$$

with the incremental (small-signal) load conductance

$$G_i \triangleq \left( \frac{1}{R_{\text{load},i}} - \frac{P^*_i}{(v^*_{c_i})^2} \right), \qquad i \in \{3,4\}. \tag{16a}$$

*(b) Linearized inductor-current.* To construct a state–space prediction model suitable for MPC, the port inductor current dynamics are approximated in an averaged form as it is shown by Eq. (17):

$$L_i \frac{d\,\overline{i}_{L_i}(t)}{dt} = -\overline{v}_{c_i}(t) - R_{L_i}\,\overline{i}_{L_i}(t) + k_{\varphi,i}\,\overline{\Delta\varphi}_i(t), \qquad i \in \{3,4\}, \tag{17}$$

where $L_i$ and $R_{L_i}$ denote the effective port inductance (H) and its lumped series resistance (Ohm), respectively. The gain $k_{\varphi,i}$ captures the sensitivity of the averaged port excitation to phase shift,

$$k_{\varphi,i} \triangleq \left. \frac{\partial v_{\text{eq},i}}{\partial \Delta\varphi_i} \right|_{(v^*_{c_i},\, i^*_{L_i},\, \Delta\varphi^*_i)}, \qquad i \in \{3,4\}, \tag{17a}$$

which can be obtained analytically from the adopted QAB steady-state power-transfer relation or numerically via small perturbation around the operating point.

*(c) State–space model and explicit matrices $A_i$, $B_i$.* For MPC design, we define the state and input vectors as Eq. (18):

$$\left\{ x_i(t) = \begin{bmatrix} \overline{v}_{c_i}(t) \\ \overline{i}_{L_i}(t) \end{bmatrix}, \qquad u_i(t) = \overline{\Delta\varphi}_i(t), \qquad i \in \{3,4\} \right. \tag{18}$$

where $\overline{(\cdot)}$ denotes small-signal (deviation) quantities around the operating point, $C_i$ is the port capacitance, $L_i$ is the equivalent series inductance, $R_{L_i}$ is the inductor series resistance, $v^*_{c_i}$ is the nominal capacitor-voltage operating point used for linearization, $k_{\varphi,i}$ is the small-signal gain relating the incremental phase shift $u_i(t) = \overline{\Delta\varphi}_i(t)$ to the inductor-current dynamics, and $G_i$ is defined in (16a).

Combining (16) and (17) gives the continuous-time linear model

$$\dot{x}_i(t) = A_i\,x_i(t) + B_i\,u_i(t) + E_i\,d_i(t), \qquad i \in \{3,4\}, \tag{19}$$

where $d_i(t) \triangleq \overline{P}_i(t)$ is the PPL power disturbance, and the matrices are explicitly as follows:

$$A_i = \begin{bmatrix} -\dfrac{G_i}{C_i} & \dfrac{1}{C_i} \\ -\dfrac{1}{L_i} & -\dfrac{R_{L_i}}{L_i} \end{bmatrix}, \qquad B_i = \begin{bmatrix} 0 \\ \dfrac{k_{\varphi,i}}{L_i} \end{bmatrix}, \qquad E_i = \begin{bmatrix} -\dfrac{1}{C_i v^*_{c_i}} \\ 0 \end{bmatrix}, \tag{19a}$$

with $G_i$ defined in (16a). Here, $x_i(t) \in \mathbb{R}^2$ is the deviation state vector (V, A), $u_i(t) \in \mathbb{R}$ is the incremental phase-shift input (rad), and $d_i(t) = \overline{P}_i(t) \in \mathbb{R}$ is the PPL power disturbance (W); $\dot{(\cdot)}$ denotes the time derivative. Accordingly, $A_i \in \mathbb{R}^{2\times2}$, $B_i \in \mathbb{R}^{2\times1}$, and $E_i \in \mathbb{R}^{2\times1}$, where $E_i$ is the disturbance-input matrix.

*(d) Discretization and prediction model.* The models in (19) are discretized using the forward Euler method with sampling period $T_s = 1 \times 10^{-3}$ s:

$$x_i(k+1) = A_{id}\,x_i(k) + B_{id}\,u_i(k) + E_{id}\,d_i(k), \qquad i \in \{3,4\}, \tag{20}$$

where

$$A_{id} = I + T_s A_i, \qquad B_{id} = T_s B_i, \qquad E_{id} = T_s E_i, \qquad i \in \{3,4\} \tag{20a}$$

where $k \in \mathbb{Z}_{\geq 0}$ denotes the discrete-time index, and $I$ is the $2 \times 2$ identity matrix (consistent with $x_i \in \mathbb{R}^2$). The prediction horizon is set to $N = 10$ steps (i.e., a prediction window of $NT_s = 10$ ms). For $j = 0, \ldots, N-1$, the predicted states evolve as

$$x_i(k+j+1|k) = A_{id}\,x_i(k+j|k) + B_{id}\,u_i(k+j|k) + E_{id}\,d_i(k+j|k). \tag{21}$$

Here, $(\cdot|k)$ denotes a quantity predicted at time instant $k$, and $j = 0, \ldots, N-1$ is the prediction-step index over the horizon $N$. Over each prediction window, $d_i(k+j|k)$ is assumed piecewise constant to capture PPL step changes.

*(e) MPC optimization (receding-horizon implementation).* At each sampling instant $k$, the control sequence $\{u_i(k|k), \ldots, u_i(k+N-1|k)\}$ is obtained by minimizing

$$\begin{aligned} J_i = &\sum_{j=0}^{N-1} \Big( x_i(k+j|k) - x_{i,\text{ref}} \Big)^\top Q_i \Big( x_i(k+j|k) - x_{i,\text{ref}} \Big) \\ &+ \sum_{j=0}^{N-1} u_i(k+j|k)^\top R_i\,u_i(k+j|k), \end{aligned} \tag{22}$$

where $J_i$ is the finite-horizon cost, $x_{i,\text{ref}} = [0\ \ 0]^\top$ is the regulation target for the deviation states, $Q_i \succeq 0$ and $R_i \succ 0$ are weighting matrices (typically $Q_i \in \mathbb{R}^{2\times2}$ and $R_i \in \mathbb{R}^{1\times1}$ for the single-input case), and $(\cdot)^\top$ denotes the transpose.

subject to the discrete-time model (21) and actuator constraints such as Eq. (23):

$$u_{i,\min} \leq u_i(k+j|k) \leq u_{i,\max}, \qquad \Delta u_{i,\min} \leq \Delta u_i(k+j|k) \leq \Delta u_{i,\max}, \tag{23}$$

where $Q_i \succeq 0$ and $R_i \succ 0$ are tuning weights, $x_{i,\text{ref}} = [0\ \ 0]^\top$ corresponds to regulation of deviations to zero, and $\Delta u_i(k) = u_i(k) - u_i(k-1)$ limits the phase-shift slew rate. Only the first optimal move is applied (receding horizon):

$$u_i(k) = u^\star_i(k|k), \qquad i \in \{3,4\}. \tag{24}$$

where $(\cdot)^\star$ denotes the optimizer of (22) subject to (21) and (23).

*(f) Integration of CMPC with ISMC (robustification).* The CMPC provides the nominal incremental phase-shift command $u^{\text{MPC}}_i(k)$ based on (20)–(24). To enhance robustness against modelling errors and fast PPL transients, the ISMC term adds a bounded corrective action:

$$\begin{aligned} u_i(k) &= u^{\text{MPC}}_i(k) + u^{\text{ISMC}}_i(k), \\ u^{\text{ISMC}}_i(k) &= -K_i\ \text{sat}\Big( \tfrac{s_i(k)}{\phi_i} \Big), \quad i \in \{3,4\}. \end{aligned} \tag{25}$$

where $s_i(k)$ is the selected sliding manifold for port $i$, $K_i > 0$ is the ISMC gain, $\phi_i > 0$ defines the boundary layer, and $\text{sat}(\cdot)$ mitigates chattering.

This CMPC–ISMC structure preserves the predictive optimal behaviour while ensuring robust disturbance rejection during pulsed-load step changes.

#### 3.0.5. Optimization-based MPC for ports 3 and 4

The MPC control action is obtained by minimizing a quadratic objective function over the prediction horizon $N$. For each port $i \in \{3,4\}$, the cost function is defined by Eq. (26):

$$\begin{cases} J^{(3)} = \sum_{k=0}^{N-1} \left( x_k^{(3)\top} Q^{(3)} x_k^{(3)} + u_k^{(3)\top} R^{(3)} u_k^{(3)} \right) + x_N^{(3)\top} \Pi^{(3)} x_N^{(3)} \\ J^{(4)} = \sum_{k=0}^{N-1} \left( x_k^{(4)\top} Q^{(4)} x_k^{(4)} + u_k^{(4)\top} R^{(4)} u_k^{(4)} \right) + x_N^{(4)\top} \Pi^{(4)} x_N^{(4)} \end{cases} \tag{26}$$

where $J^{(i)}$ is the MPC objective function for port $i$, $x_k^{(i)}$ and $u_k^{(i)}$ are the predicted state and input at prediction step $k$, and $(\cdot)^\top$ denotes the transpose operator. The matrices $Q^{(i)} \succeq 0$ and $R^{(i)} \succ 0$ are the state- and input-weighting matrices, respectively, and $\Pi^{(i)} \succeq 0$ is the terminal-state weighting matrix. For the state definition in Eq. (26), $x_k^{(i)} \in \mathbb{R}^2$ and $u_k^{(i)} \in \mathbb{R}$ [37].

MPC weight selection: The MPC weights were selected by (i) normalizing the states and input by their expected operating ranges, (ii) initializing the weights using a Bryson-type guideline, and (iii) refining them through a brief parametric sweep under representative 100–200 W PPLs steps to balance fast voltage recovery against limited control effort. In this research, scalar weights were used (since $x_k^{(i)} \in \mathbb{R}^2$ and $u_k^{(i)} \in \mathbb{R}$), and the same set was adopted for ports 3 and 4 for symmetry. The final values are $Q^{(3)} = Q^{(4)} = 1$, $R^{(3)} = R^{(4)} = 0.1$, and $\Pi^{(3)} = \Pi^{(4)} = 2.2367$.

Sensitivity: Increasing $Q^{(i)}$ improves tracking speed (faster voltage recovery) but increases actuation effort and current stress, whereas increasing $R^{(i)}$ yields smoother control action at the expense of slower recovery.

#### 3.0.6. Sequential control execution in MPC

At each sample, apply only the first optimal move (receding horizon) (27):

$$\begin{cases} u_{\mathrm{MPC},3} = u_0^*(t_k), & t \in [\,t_k,\, t_{k+1}\,] \\ u_{\mathrm{MPC},4} = u_0^*(t_k), & t \in [\,t_k,\, t_{k+1}\,] \end{cases} \tag{27}$$

terminal sets $\mathcal{X}_{N,i}$ ensure recursive feasibility/stability. The final CMPC –ISMC input adds ISMC terms (Eq. (10)) for ports 3 and 4 (28):

$$\begin{cases} u_3(t) = u_{\mathrm{MPC},3}(t) + u_{\mathrm{ISMC},3}(t) \\ u_4(t) = u_{\mathrm{MPC},4}(t) + u_{\mathrm{ISMC},4}(t) \end{cases} \tag{28}$$

Eq. (28) represents the core composite control law of the proposed CMPC–ISMC scheme, where the smooth predictive action $u_{\mathrm{MPC},i}(t)$ is augmented by the robust corrective term $u_{\mathrm{ISMC},i}(t)$ to improve tracking and disturbance rejection. The resulting $u_i(t)$ is then used to generate the phase-shift command applied to the PWM modulator (subject to practical saturation/decoupling constraints where applicable).

### 3.1. Adaptive Suboptimal Second-Order Sliding Mode Controller (ASSO SMC)

The ASSOSMC is a nonlinear control strategy that ensures finite-time convergence of both the output error and its derivative, while significantly reducing the chattering typically associated with classical Sliding Mode Control (SMC) [36,38]. For ports 3–4 Fig. 1, Eq. (1), define sliding variables (29) and their dynamics (30):

$$\begin{cases} \sigma_3(t) = v_{c_3}(t) - v_{c_3}^* \\ \sigma_4(t) = v_{c_4}(t) - v_{c_4}^* \end{cases} \tag{29}$$

$$\begin{cases} \dot{\sigma}_3(t) = \dfrac{1}{C_3} \left[ i_{L_3}(t) - \dfrac{v_{c_3}(t)}{R_{\mathrm{load},3}} - \dfrac{P_{\mathrm{PPL},3}}{v_{c_3}(t)} \right] - \dot{v}_{c_3}^*(t) \\ \dot{\sigma}_4(t) = \dfrac{1}{C_4} \left[ i_{L_4}(t) - \dfrac{v_{c_4}(t)}{R_{\mathrm{load},4}} - \dfrac{P_{\mathrm{PPL},4}}{v_{c_4}(t)} \right] - \dot{v}_{c_4}^*(t) \end{cases} \tag{30}$$

let auxiliary variables (31), (32) and adaptive gain $\alpha_i(t)$ (33) shape the sliding action; choose $\beta_i$ per (34) to dominate uncertainties $\varsigma_i$:

$$\zeta_{1,i}(t) = \sigma_i(t) \tag{31}$$

$$\zeta_{2,i}(t) = \dot{\sigma}_i(t) \tag{32}$$

where $\zeta_{1,i}(t)$ is the sliding variable, and $\zeta_{2,i}(t)$ represents the derivative of the sliding variable, with $i \in \{3,4\}$ corresponding to ports 3 and 4. To enhance performance and reduce chattering, an adaptive gain parameter $\alpha_i(t)$ is introduced, as expressed in Eq. (33):

$$\alpha_i(t) = \begin{cases} \alpha^*, & \text{if } \left(\zeta_{1,i}(t) - \frac{1}{2}\zeta_{\max,i}(t)\right)\left(\zeta_{\max,i}(t) - \zeta_{1,i}(t)\right) > 0, \\ 1, & \text{otherwise.} \end{cases} \tag{33}$$

To ensure a sufficiently strong sliding motion, the parameters $\beta_3$ and $\beta_4$ in ASSOSMC are defined as follows Eq. (34):

$$\begin{cases} \beta_3 > \max\left( \dfrac{\varsigma_3}{\alpha_3 \vartheta_{\min}}, \dfrac{4\varsigma_3}{3\vartheta_{\min} - \alpha_3(t)\vartheta_{\max}} \right), \\ \beta_4 > \max\left( \dfrac{\varsigma_4}{\alpha_4 \vartheta_{\min}}, \dfrac{4\varsigma_4}{3\vartheta_{\min} - \alpha_4(t)\vartheta_{\max}} \right), \end{cases} \tag{34}$$

where $\vartheta_{\min}$ and $\vartheta_{\max}$ denote the lower and upper bounds of the function $\vartheta_i(t)$, with $i \in \{3,4\}$ corresponding to ports 3 and 4. The requirements and inequality conditions for $\beta_3$ and $\beta_4$ are specified in detail in the design section [36]. Chattering is mitigated by replacing the ideal discontinuous $\mathrm{sign}(\cdot)$ with the boundary-layer saturation function $\mathrm{sat}(\cdot)$. The saturation function is defined as

$$\mathrm{sat}(x) = \begin{cases} 1, & x > 1, \\ x, & |x| \le 1, \\ -1, & x < -1\ . \end{cases}$$

The final control law of the ASSOSMC for ports 3 and 4 is obtained by combining Eqs. (33) and (34), yielding the expression shown in Eq. (35):

$$\begin{cases} u_3(k) = -\,\mu_3\, \beta_3\ \mathrm{sat}\left( \dfrac{\zeta_{1,3}(k) - \frac{1}{2}\,\zeta_{\max,3}}{\delta_3} \right) \\ u_4(k) = -\,\mu_4\, \beta_4\ \mathrm{sat}\left( \dfrac{\zeta_{1,4}(k) - \frac{1}{2}\,\zeta_{\max,4}}{\delta_4} \right) \end{cases}, \tag{35}$$

where $\delta_3 > 0$ and $\delta_4 > 0$ are the boundary-layer thicknesses,

where $k$ is the discrete-time index ($t = kT_s$, with sampling period $T_s$), and $u_3(k)$ and $u_4(k)$ are the ASSOSMC control inputs applied to ports 3 and 4, respectively (held constant over each sampling interval via a zero-order hold).

The variables $\zeta_{1,3}(k)$ and $\zeta_{1,4}(k)$ denote the sliding variables (first SOSM auxiliary variables) for ports 3 and 4, and $\zeta_{\max,3} > 0$ and $\zeta_{\max,4} > 0$ are their estimated maximum bounds used to regulate the switching threshold and control effort. The parameters $\mu_3 > 0$ and $\mu_4 > 0$ are scaling gains, while $\beta_3 > 0$ and $\beta_4 > 0$ are robustness gains selected to dominate bounded modelling uncertainties and disturbance terms.

#### 3.1.1. Integral Higher-Order Sliding Mode Controller (IHOSMC)

In QAB resonant converters supplying PPLs, IHOSMC shows reduced robustness due to a slow or unpredictable reaching phase, degraded transient response with potential overshoot or oscillations, and highly variable reaching times when subjected to noise, delays, and switching

constraints despite mitigation of chattering issues . Therefore, it is essential to benchmark IHOSMC against other robust control strategies under PPLs [39,40]. Define tracking errors (36) based on Fig. 1 and use capacitor dynamics to get Eq. (37):

$$\begin{cases} \varrho_3(t) = v_{c_3}(t) - v_{c_3}^{\text{ref}} \\ \varrho_4(t) = v_{c_4}(t) - v_{c_4}^{\text{ref}} \end{cases} \tag{36}$$

from the capacitor dynamics for ports 3 and 4, the following Eq. (37) can be defined as follows:

$$\begin{cases} \dfrac{d\varrho_3(t)}{dt} = \dfrac{dv_{c_3}(t)}{dt} - \dfrac{1}{C_3}\left(i_{L_3}(t) - \dfrac{v_{c_3}(t)}{R_{\text{load},3}} - \dfrac{P_{\text{PPL},3}}{v_{c_3}(t)}\right) \\ \dfrac{d\varrho_4(t)}{dt} = \dfrac{dv_{c_4}(t)}{dt} - \dfrac{1}{C_4}\left(i_{L_4}(t) - \dfrac{v_{c_4}(t)}{R_{\text{load},4}} - \dfrac{P_{\text{PPL},4}}{v_{c_4}(t)}\right) \end{cases} \tag{37}$$

assume inductor currents in control-affine form (38) and recast as (39), (40) with bounded $f_{1,i}, f_{2,i}$:

$$i_{L_i}(t) = g_i(t)\,u_i(t) + b_i(t) \tag{38}$$

$$\left\{ \frac{d\varrho_i}{dt} = \frac{1}{C_i}\left(g_i u_i + b_i - \frac{v_{c_i}}{R_{\text{load},i}} - \frac{P_{\text{PPL},i}}{v_{c_i}}\right) - \dot{v}_{c_i}^{\text{ref}}(t) \right. \tag{39}$$

where $u_i(t)$ is the control variable for port $i \in \{3,4\}$, $g_i(t)$ is the effective control gain (which depends on the operating point of the system), and $b_i(t)$ is the lumped uncertainty term.

$$\frac{d\varrho_i(t)}{dt} = f_{1,i}(t) + f_{2,i}(t)\,u_i(t). \tag{40}$$

$$f_{1,i}(t) = \frac{1}{C_i}\left(b_i(t) - \left(\frac{v_{c_i}(t)}{R_{\text{load},i}} + \frac{P_{\text{PPL},i}}{v_{c_i}(t)}\right)\right) \in [-H_i,\ H_i], \qquad i \in \{3,4\}, \tag{40a}$$

$$f_{2,i}(t) = \frac{1}{C_i}\,g_i(t) \in \left[g_{\min,i},\ g_{\max,i}\right], \qquad i \in \{3,4\}. \tag{40b}$$

where $v_{c_i}(t)$ is the capacitor voltage at port $i$, $R_{\text{load},i}$ is the fixed resistive load, $P_{\text{PPL},i}$ is the pulsed-power-load (PPL) power, $b_i(t)$ is the lumped uncertainty/disturbance term, $g_i(t)$ is the effective control gain, and $C_i$ denotes the output capacitance at port $i$ with $C_3 = C_4 = 1.29 \times 10^{-6}$ F. The bound $H_i$ is defined as $H_i = \max_t \left|f_{1,i}(t)\right|$, and the control-gain bounds are chosen as $g_{\min,i} = 0.7$ and $g_{\max,i} = 1.35$.

To mitigate chattering, replace the sign law (41) with a saturation-based reaching law (42), (43):

$$\dot{u}_i(t) = -K_i\ \text{sign}\big(\xi_i(t)\big) \tag{41}$$

while this formulation ensures robustness, it introduces chattering that can degrade control performance, even for $K_i > 0$. To mitigate this issue, the discontinuous sign function $\text{sign}\big(\xi_i(t)\big)$ in Eq. (41) is replaced by a continuous saturation function, defined in Eq. (42).

$$\text{sat}\left(\frac{\xi_i(t)}{\phi}\right) = \begin{cases} 1, & \xi_i/\phi > 1, \\ \xi_i/\phi, & |\xi_i/\phi| \le 1, \\ -1, & \xi_i/\phi < -1, \end{cases} \tag{42}$$

$$\begin{cases} \dot{\xi}_3(t) = -K_3\ \text{sat}\left(\dfrac{\xi_3(t)}{\phi}\right) \\ \dot{\xi}_4(t) = -K_4\ \text{sat}\left(\dfrac{\xi_4(t)}{\phi}\right) \end{cases} \tag{43}$$

where $K_3 = K_4 = 257$ are the control gains for ports 3 and 4, and $\phi > 0$ is the boundary-layer parameter used to reduce chattering. define the integral higher-order surface Eqs. (44)–(45) with gains $\gamma_{1,2,3}$:

$$\xi_i(t) = \gamma_1 \int_0^t \varrho_i(\tau)\,d\tau + \gamma_2\,\varrho_i(t) + \gamma_3\,\frac{d\varrho_i(t)}{dt} \tag{44}$$

$$\dot{\xi}_i(t) = \gamma_1\,\varrho_i(t) + \gamma_2\,\dot{\varrho}_i(t) + \gamma_3\,\ddot{\varrho}_i(t). \tag{45}$$

This ensures a smooth and reliable signal for use in the IHOSMC control law. Since the control algorithm operates in discrete time, only a finite set of sampled data points, e.g., $\varrho_i(t)$, $\varrho_i(t - \Delta t)$, and $\varrho_i(t - 2\Delta t)$, is available. Accordingly, a Taylor-series-based approximation is employed, and the first derivative of the tracking error is computed as in Eq. (46) and a first-order filter Eqs. (46)–(47) and (48):

$$\dot{\varrho}_i(t) \approx \frac{\varrho_i(t) - \varrho_i(t - \Delta t)}{\Delta t}. \tag{46}$$

then, the second derivative is estimated as well by Eq. (47)

$$\frac{d^2\varrho_i(t)}{dt^2} \approx \frac{\dfrac{d\varrho_i(t)}{dt} - \dfrac{d\varrho_i(t - \Delta t)}{dt}}{\Delta t} \tag{47}$$

to further suppress noise and achieve a smooth signal, the second derivative is passed through a first-order low-pass filter and provides Eq. (48):

$$\left(\frac{d^2\varrho_i}{dt^2}\right)_{\text{filt}} = (1 - \vartheta)\left(\frac{d^2\varrho_i}{dt^2}\right)(t - \Delta t) + \alpha\,\frac{d^2\varrho_i(t)}{dt^2}, \tag{48}$$

with $\alpha = \frac{T_s}{\tau + T_s}$, $\tau = 10^{-3}$, $\Delta t = T_s$, equating the surface dynamics to the reaching law yields Eqs. (49)–(50):

$$\gamma_1\,\varrho_i + \gamma_2\,\dot{\varrho}_i + \gamma_3\,\ddot{\varrho}_i = -K_i\ \text{sat}\left(\frac{\xi_i}{\phi}\right) \tag{49}$$

$$\ddot{\varrho}_i = \frac{-K_i\ \text{sat}\left(\frac{\xi_i}{\phi}\right) - \gamma_1\,\varrho_i - \gamma_2\,\dot{\varrho}_i}{\gamma_3} \tag{50}$$

using the control-affine form Eqs. (51)–(52),

$$\dot{\varrho}_i = f_{1,i} + f_{2,i}\,u_i, \tag{51}$$

$$u_i = \frac{\dot{\varrho}_i - f_{1,i}}{f_{2,i}}, \tag{52}$$

and substituting into the surface dynamics gives the final IHOSMC inputs Eqs. (53), (54) and (55):

$$\gamma_1\,\varrho_i + \gamma_2\big(f_{1,i} + f_{2,i}\,u_i\big) + \gamma_3\,\ddot{\varrho}_i = -K_i\ \text{sat}\left(\frac{\xi_i}{\phi}\right) \tag{53}$$

By rearranging Eq. (53) to isolate the control input $u_i(t)$ and dividing both sides by $\gamma_2\,f_{2,i}(t)$, the final control laws for ports 3 and 4, i.e., Eqs. (54) and (55) are obtained.

$$u_3 = \frac{-f_{1,3} - \gamma_1\,\varrho_3 - \gamma_2\,\frac{d\varrho_3}{dt} - \gamma_3\,\frac{d^2\varrho_3}{dt^2} - K_3\ \text{sat}\left(\frac{\xi_3}{\phi}\right)}{f_{2,3}} \tag{54}$$

$$u_4 = \frac{-f_{1,4} - \gamma_1\,\varrho_4 - \gamma_2\,\frac{d\varrho_4}{dt} - \gamma_3\,\frac{d^2\varrho_4}{dt^2} - K_4\ \text{sat}\left(\frac{\xi_4}{\phi}\right)}{f_{2,4}} \tag{55}$$

where $u_i$ is the port inputs $i \in \{3,4\}$, $f_{1,i}$ cancels matched disturbances, $f_{2,i}$ normalizes the control by the (bounded) gain, and $\gamma_{1,2,3}, K_i, \phi$ shape the IHOSMC transient and chattering trade-offs.

To avoid the singularity in the pulsed power load (PPLs) model $i_{\text{PPL},i}(t) = P_{\text{PPL},i}(t)/v_{c_i}(t)$ as $v_{c_i}(t) \to 0$, the denominator is regularized using a minimum-voltage threshold $v_{\min} = 5\,\text{V}$. Specifically, an effective voltage $\tilde{v}_{c_i}(t) = \max\big(v_{c_i}(t), 5\,\text{V}\big)$ is used so that $i_{\text{PPL},i}(t) = P_{\text{PPL},i}(t)/\tilde{v}_{c_i}(t)$ remains bounded during large disturbances. This safeguard is applied consistently in both the simulations and the OPAL-RT hardware-in-the-loop implementation.

### 3.1.2. Decoupling controller for inter-port coupling compensation

Although the ISMC laws in (10) generate the required (virtual) control inputs $u_{\text{ISMC},3}(t)$ and $u_{\text{ISMC},4}(t)$, the QAB exhibits strong inter-port coupling through the multiwinding transformer and resonant network [11]. Therefore, a 2 × 2 feedforward decoupling block is introduced to map the two control channels into physically realizable PWM phase-shift commands.why this error

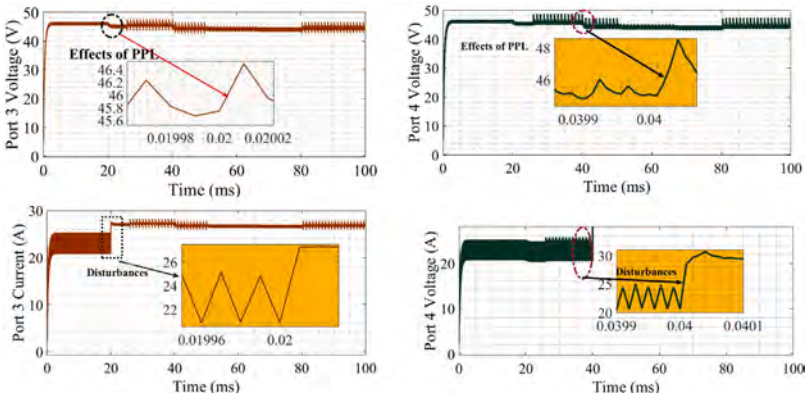


**Fig. 3.** Voltage and Current for ports 3 and 4 under PI and feedforward decoupling.

*Step 1: Define the virtual control vector.* From (10), define the ISMC virtual control vector for ports 3 and 4 as

$$\mathbf{u}(t) = \begin{bmatrix} u_{\mathrm{ISMC},3}(t) \\ u_{\mathrm{ISMC},4}(t) \end{bmatrix}. \tag{56}$$

*Step 2: Coupled small-signal current–phase model.* Around an operating point $\boldsymbol{\phi}^\star = \begin{bmatrix} \phi_3^\star & \phi_4^\star \end{bmatrix}^\top$, the coupled QAB port-current variations can be locally approximated by

$$\Delta \mathbf{i}_L(t) = G\,\Delta\boldsymbol{\phi}(t), \qquad \Delta \mathbf{i}_L(t) = \begin{bmatrix} \Delta i_{L_3}(t) \\ \Delta i_{L_4}(t) \end{bmatrix}, \quad \Delta\boldsymbol{\phi}(t) = \begin{bmatrix} \Delta\phi_3(t) \\ \Delta\phi_4(t) \end{bmatrix}. \tag{57}$$

where the coupling matrix $G$ is the Jacobian which is detailed in [11, 20,41]:

$$G = \begin{bmatrix} g_{33} & g_{34} \\ g_{43} & g_{44} \end{bmatrix} = \left[ \begin{array}{cc} \dfrac{\partial i_{L_3}}{\partial \phi_3} & \dfrac{\partial i_{L_3}}{\partial \phi_4} \\ \dfrac{\partial i_{L_4}}{\partial \phi_3} & \dfrac{\partial i_{L_4}}{\partial \phi_4} \end{array} \right]_{\boldsymbol{\phi}^\star}. \tag{58}$$

Here, $g_{33}$ and $g_{44}$ are the direct gains, whereas $g_{34}$ and $g_{43}$ capture cross-coupling between ports 3 and 4.

*Step 3: Feedforward decoupling law.* To reduce interaction, the decoupler computes the phase-shift corrections using

$$\Delta\boldsymbol{\phi}(t) = H\,\Delta\mathbf{i}_c(t), \qquad H = G^{-1}, \tag{59}$$

where $\Delta\mathbf{i}_c(t)$ is the two-channel current command entering the decoupler. In this work, $\Delta\mathbf{i}_c(t)$ is taken as the ISMC virtual control vector, i.e., $\Delta\mathbf{i}_c(t) = \mathbf{u}(t)$.

For the $2 \times 2$ case, the determinant of $G$ is

$$\det(G) = g_{33}g_{44} - g_{34}g_{43}, \tag{60}$$

and the decoupling matrix can be written explicitly as

$$H = \frac{1}{\det(G)} \begin{bmatrix} g_{44} & -g_{34} \\ -g_{43} & g_{33} \end{bmatrix} = \begin{bmatrix} A & B \\ C & D \end{bmatrix}. \tag{61}$$

Therefore, the decoupled phase-shift corrections (the Mux–matrix block) are computed as follows:

$$\begin{cases} \Delta\phi_3(t) = A\,u_{\mathrm{ISMC},3}(t) + B\,u_{\mathrm{ISMC},4}(t), \\ \Delta\phi_4(t) = C\,u_{\mathrm{ISMC},3}(t) + D\,u_{\mathrm{ISMC},4}(t). \end{cases} \tag{62}$$

*Step 4: Regularized decoupling.* When $G$ is ill-conditioned, a damped least-squares decoupler can be used:

$$H_\lambda = (G^\top G + \lambda I)^{-1} G^\top, \qquad \lambda > 0, \tag{63}$$

and $H$ in Eq. (59) is replaced by $H_\lambda$.

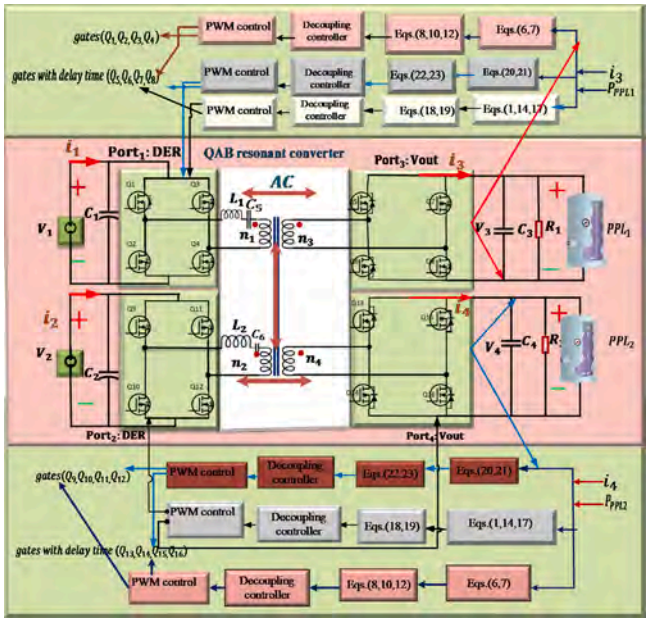


**Fig. 4.** QAB converter with nonlinear controllers.

*Step 5: Phase saturation and PWM generation.* Finally, the PWM phase-shift commands are obtained by adding the corrections to the nominal phase shifts and applying saturation limits:

$$\begin{cases} \phi_3(t) = \phi_3^\star + \mathrm{sat}_{\Delta\phi_{\max}}\big(\Delta\phi_3(t)\big), \\ \phi_4(t) = \phi_4^\star + \mathrm{sat}_{\Delta\phi_{\max}}\big(\Delta\phi_4(t)\big). \end{cases} \tag{64}$$

where $\Delta\phi_{\max}$ denotes the maximum allowable phase deviation and the resulting $\phi_3(t)$ and $\phi_4(t)$ are passed to the PWM block to generate the gate signals.

### 3.1.3. Baseline controller: Conventional PI with feedforward decoupling

Fig. 3 shows the Port 3 and Port 4 voltage and current responses after implementing a PI controller with feedforward decoupling. At $t = 0.02$ s, the PPL disturbance causes the Port 3 voltage to drop to 44.5 V and the Port 3 current to rise to 27.5 A. At $t = 0.04$ s, the Port 4 voltage decreases to 44.2 V while the Port 4 current increases to 30 A. Although the PI controller maintains regulation during PPL operation, coupling effects between the ports remain [42].

Fig. 4 illustrates the main diagram of the QAB resonant converter incorporating three controllers: CMPC with ISMC, ASSOSMC, and IHOSMC. Each applied separately with feedforward decoupling control for a decoupled QAB converter.

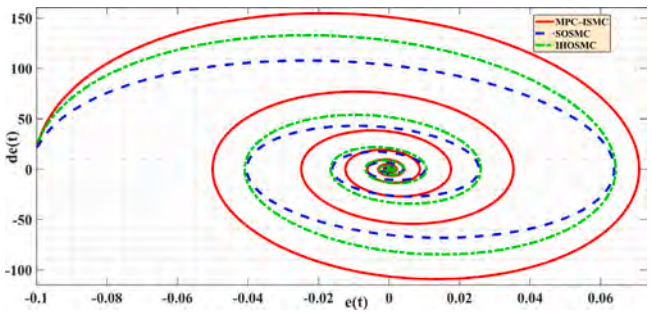


**Fig. 5.** State–space trajectories for controllers for ports 3 and 4.

## 4. Simulation results

To ensure stable voltage tracking under PPL conditions, the QAB resonant converter is tested with three nonlinear controllers: ASSOSMC, IHOSMC, and CMPC with ISMC. Together, they target constraint-aware optimization (CMPC with ISMC), fast dynamics with reduced chattering (ASSOSMC), and robustness via higher-order sliding behaviour (IHOSMC), enabling stable regulation under rapid load transients.

### 4.1. Estimated state space-trajectories

Fig. 5 shows that IHOSMC begins with a substantial initial error and exhibits sharp directional changes, indicating strong corrective action and potential chattering near the sliding surface. In contrast, CMPC–ISMC demonstrates a smooth, spiral-like convergence, reflecting its predictive nature and well-damped response. Adaptive ASSOSMC starts closer to the vertical axis and achieves rapid, stable convergence with minimal oscillation, effectively balancing speed and robustness, making it well-suited for regulating ports that supply pulsed power loads.

### 4.2. Simulation results of the ASSOSMC controller

Fig. 6 shows voltage deviations $\Delta V_3 = 0.5$ V; $\Delta V_4 = 0.3$ V, at 1 s and load currents for ports 3 and 4 $I_i = 5$ A, control law input variations $\Delta u_3 = 0.05$ V to $-0.02$ V at 2 s, and $\Delta u_4 = -0.03$ V because of PPLs increased from 100 W to 200 W. Thus, the dynamic characteristics include rise times of 6 µs, rise time of 8 µs for control inputs, fall time of 200 ms, settling time 3.6 µs, preshoot (0.5–32.66%) and overshoot (0.7–1.531%).

Fig. 7 illustrates the control input behaviour at ports 3 and 4 during PPL disturbances. At port 3, the PPL increases from 100 W to 200 W at 1 s, while at port 4, it increases from 100 W to 200 W after 2 s.

The response exhibits a rise time of 8 µs, a settling time of 4.7 µs, a preshoot of 0.667%, and an overshoot of 0.2427%. The control input $u_3$ rises to 0.05 V and drops to $-0.02$ V after 2 s, whereas $u_4$ changes to $-0.03$ V in response to the load increase.

### 4.3. Simulation results of the IHOSMC controller

Fig. 8 depicts the control input behaviour at ports 3 and 4 during PPL disturbances. At port 3, the PPL increases from 100 W to 200 W at 1 s, while at port 4, it increases from 100 W to 200 W after 2 s. The response exhibits a rise time of 6 µs, a settling time of 4.7 µs, a fall time 200 ms a preshoot of 22.66%, and an overshoot of 0.667%. Consequently, the voltage at port 3 decreases by 3 V with a current $\mathbf{I}_3 = 2.5$ A while the voltage at port 4 drops by 2.8 V over 2 s with a current $I_4 = 2.6$ A.

Fig. 9 illustrates the control input behaviour at ports 3 and 4 during PPL disturbances. At port 3, the PPL increases from 100 W to 200 W at 1 s, while at port 4, it rises from 100 W to 200 W at 2 s,. The response features a rise time of 987 µs, a preshoot of 0.5%, an overshoot of $-1.476$%, and an undershoot of 21.58%. The control input $u_3$ changes to 1.2 V and then drops to $-2$ V at 2 s, whereas $u_4$ increases from 1.5 V to 2.1 V at 2 s in response to the load increase.

### 4.4. Simulation results of the CMPC with ISMC controller

Fig. 10 illustrates the performance of the CMPC combined with an ISMC controller during PPL disturbances, where the load increases from 100 W to 200 W at $1-2$ s.

The response exhibits a rise time of 7 µs, a fall time of 200 ms, a preshoot of 22.667%, an overshoot of 0.667%, and a settling time of 3.6 µs. Consequently, the voltage at ports 3 decreases by 3.5 V with a current of $I_3 = 2.4$ A, while the voltage at port 4 drops by 4.2 V over 2 s with a current of $I_4 = 2.5$ A.

Fig. 11 shows the control inputs for ports 3 and 4 along with their respective active power levels. The response is characterized by a rise time of 1.007 ms, a preshoot of 0.510%, an overshoot of 1.532% corresponding to a PPL increase from 100 W to 200 W. The control input $U_3$ changes to 0.2 V and then decreases to $-0.1$ V at 2 s, while $U_4$ varies from 0.25 V to 0.4 V as the load increases.

Table 3 compares ASSOSMC, CMPC–ISMC, and IHOSMC using MATLAB simulation results. ASSOSMC achieves accurate voltage tracking but with higher current and preshoot, while CMPC–ISMC provides smoother and more energy-efficient regulation. IHOSMC offers a balanced trade-off, motivating the subsequent experimental validation.

*Efficiency and current-stress metrics.* To quantify the energy performance, the overall conversion efficiency and total loss are computed from the logged port-power signals over the same steady-state window used for waveform analysis ($t = 2.1166$–$2.8610$ s) as

$$\eta_{\text{tot}} = \frac{P_{\text{out},3} + P_{\text{out},4}}{P_{\text{in},1} + P_{\text{in},2}}, \qquad P_{\text{loss,tot}} = (P_{\text{in},1} + P_{\text{in},2}) - (P_{\text{out},3} + P_{\text{out},4}). \tag{65}$$

In addition, RMS currents are reported to quantify current stress under PPL disturbances using $\mathbf{I}_{\text{rms}} = [I_{\text{in1,rms}}, I_{\text{in2,rms}}, I_{3,\text{rms}}, I_{4,\text{rms}}]$, where $I_{3,\text{rms}}$ and $I_{4,\text{rms}}$ denote the RMS port currents at ports 3 and 4, respectively.

Over this interval, CMPC–ISMC achieves the highest efficiency, $\eta_{\text{tot}} = 90.775$%, with $\overline{P}_{\text{in,tot}} = 2167.739$ W, $\overline{P}_{\text{out,tot}} = 1967.755$ W, and $\overline{P}_{\text{loss,tot}} = 199.984$ W. ASSOSMC attains a comparable efficiency of $\eta_{\text{tot}} = 90.724$% with $\overline{P}_{\text{loss,tot}} = 186.206$ W, whereas IHOSMC yields $\eta_{\text{tot}} = 89.055$% with $\overline{P}_{\text{loss,tot}} = 309.273$ W. The corresponding RMS-current vectors (in A) are

$$\mathbf{I}_{\text{rms}}^{\text{CMPC–ISMC}} = (4.868, 4.868, 20.484, 19.476)\,\text{A},$$
$$\mathbf{I}_{\text{rms}}^{\text{ASSOSMC}} = (4.534, 4.533, 10.251, 26.626)\,\text{A},$$
$$\mathbf{I}_{\text{rms}}^{\text{IHOSMC}} = (6.239, 6.239, 26.203, 26.127)\,\text{A}.$$

These metrics support a consistent comparative interpretation: CMPC–ISMC provides the best efficiency and reduces RMS current stress relative to IHOSMC on both regulated ports (notably $I_{4,\text{rms}}$), while ASSOSMC achieves comparable efficiency with a lower $I_{3,\text{rms}}$ but a higher $I_{4,\text{rms}}$, indicating a less balanced port-current distribution under the same PPL disturbance.

### 4.5. Experimental results

The ASSOSMC performance is experimentally validated using HIL testing on an OPAL-RT OP5700 real-time simulator. For a fair comparison, it is benchmarked against IHOSMC and CMPC–ISMC. Fig. 12 shows the experimental setup used for high-fidelity testing under realistic power-converter operating conditions.

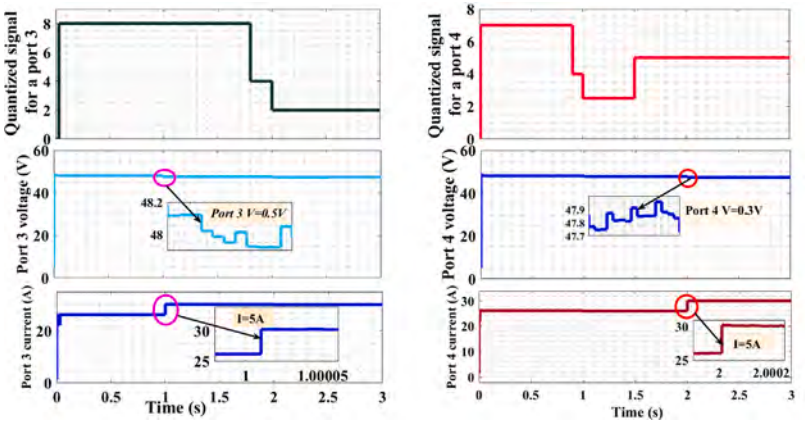


**Fig. 6.** Voltage and current at ports 3 and 4 under disturbances.

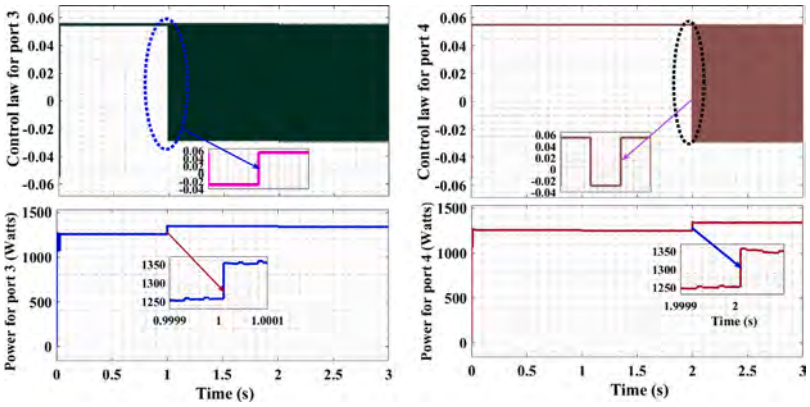


**Fig. 7.** Control input for ports 3 and 4 under disturbances.

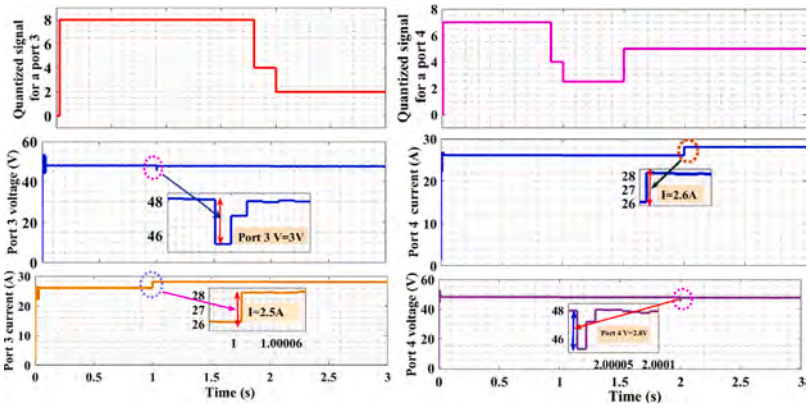


**Fig. 8.** Voltage and current at ports 3 and 4 under disturbances.

**Table 3**
Performance analysis of ASSOSMC, CMPC with ISMC and IHOSMCcontrollers.

| Criteria | ASSOSMC | IHOSMC | CMPC–ISMC |
|---|---|---|---|
| Voltage regulation | Best ($\Delta V < 1$ V) | Medium ($\Delta V \approx 3$ V) | Least accurate ($\Delta V \approx 4.2$ V) |
| Current draw | High (5 A) | Moderate (2.5 A) | Lowest (2.4–2.5 A) |
| Control input | Smallest variations | Largest variations | Moderate and stable |
| Settling/Rise time | Fastest | Fastest | Slower (1 ms on $u$) |
| Preshoot/Overshoot | Highest preshoot (23%) | High preshoot + undershoot | Lowest on control input |
| Robustness | Tight voltage regulation and high current | Balanced | Adaptive and soft rejection |

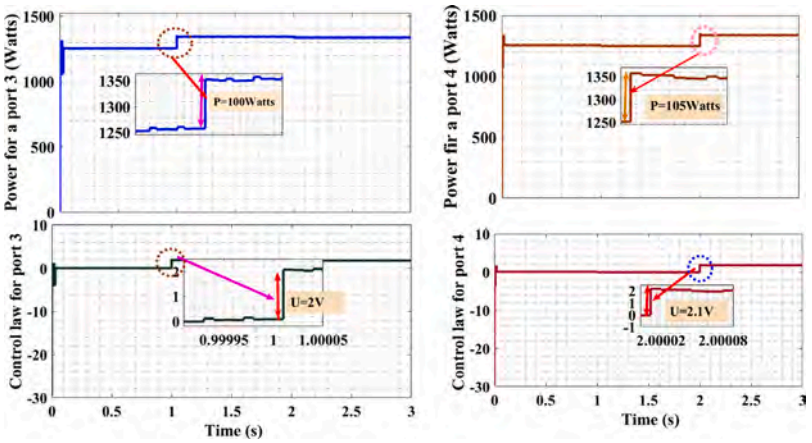


**Fig. 9.** Control input for ports 3 and 4 under disturbances.

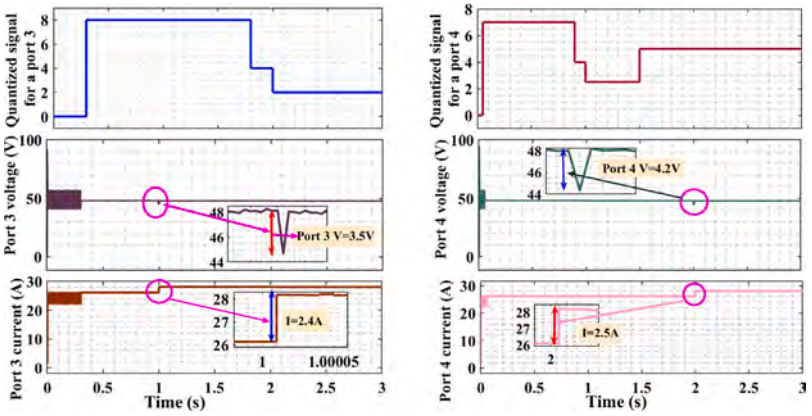


**Fig. 10.** Voltage and current at ports 3 and 4 under disturbances.

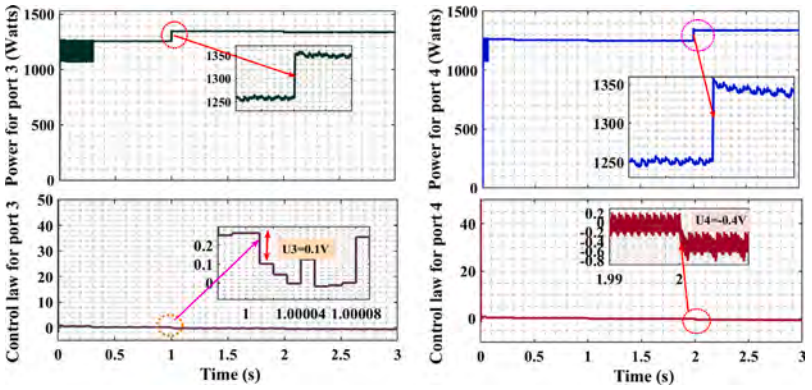


**Fig. 11.** Control input for ports 3 and 4 under disturbances.

*4.5.1. Results obtained of the ASSOSMC controller*

Fig. 13 shows the ASSOSMC experimental active-power transfer under PPL stair excitation. When the PPL is connected, the transferred power increases rapidly: $P_{1\to3}$ rises from 1076 W to 1265 W at 0.03 s and further to 1440 W after the 100–200 W PPL step at 2 s. Similarly, $P_{2\to4}$ increases from 1076 W to 1265 W at 0.01 s and reaches 1405 W following the PPL step at 2 s, remaining below the rated limit of 1500 W. These results confirm that ASSOSMC sustains stable power transfer and handles fast PPL transients while respecting the converter power rating.

Figs. 14 and 15 show the SST waveforms between Ports 1 and 3 of the QAB converter. The input voltage is 300 V (scaled by 1/30), and the output voltage is 48 V (scaled by 1/5). The measured delay is $25 \times 10^{-8}$ s between Ports 1 and 3, and $28 \times 10^{-7}$ s between Ports 2 and 4. The inductor current is approximately 30 A (scaled by 1/5) under SST operation.

*4.5.2. Results obtained of the CMPC with ISMC controller*

Fig. 16 shows that the power between $P_{1\to3}$ rises from 1070 W to 1260 W at 0.03 s and reaches 1345 W during the subsequent 100–200 W PPL increase, while $P_{2\to4}$ increases from 1080 W to 1260 W at 0.01 s. Energy efficiency is evaluated over a common steady-state averaging interval ($t \in [2.1166, 2.8610]$ s) using $\eta = P_{out}/P_{in} \times 100\%$. Based on the recorded averaged input/output powers, CMPC–ISMC achieves the

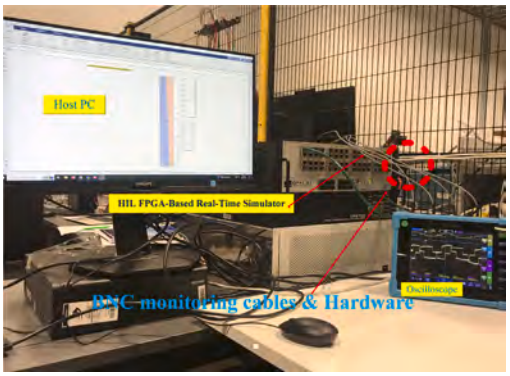


**Fig. 12.** Experimental setup for validating the proposed controller.

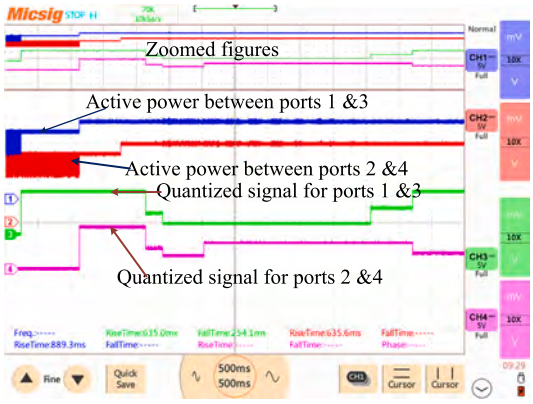


**Fig. 13.** Active power between ports and quantized signals.

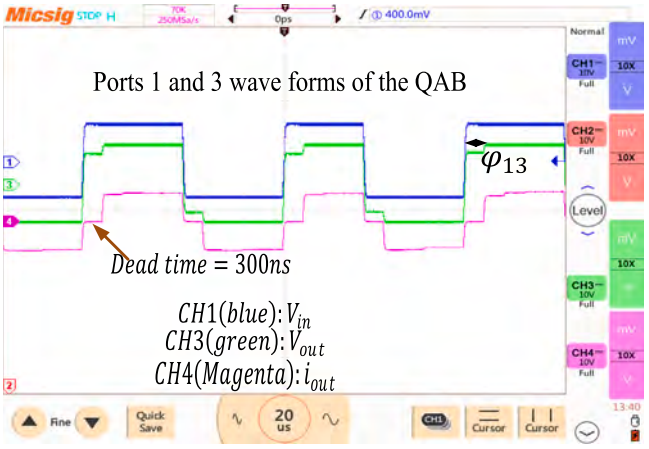


**Fig. 14.** QAB waveforms at Ports 1 and 3 under ASSOSMC.

highest efficiency ($\eta \approx 90.775\%$), followed closely by ASSOSMC ($\eta \approx 90.724\%$), whereas IHOSMC yields a lower efficiency of $\eta \approx 89.055\%$.

Figs. 17, and 18 illustrate the characteristics of the SST with a 300 V input (scaled by a factor of 1/27) and a 48 V output voltage (scaled by 1/5). The system incorporates a 350 ns dead time between switching events and inter-bridge phase shifts ranging from 0.01 to 0.05 rad.

### 4.5.3. Results obtained of the IHOSMC controller

Fig. 19 presents the IHOSMC experimental active-power transfer under PPL stair excitation. When the PPL is connected, the transferred power increases rapidly: $P_{1\to3}$ rises from 1080 W to 1260 W at 0.03 s and further to 1350 W during the subsequent PPL increase (100–200 W).

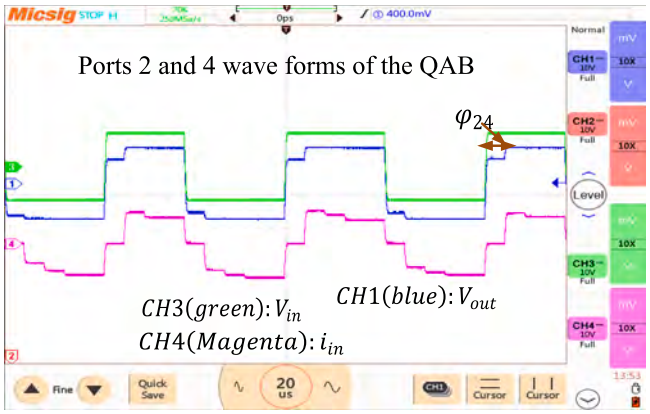


**Fig. 15.** QAB waveforms at ports 2 and 4 under ASSOSMC.

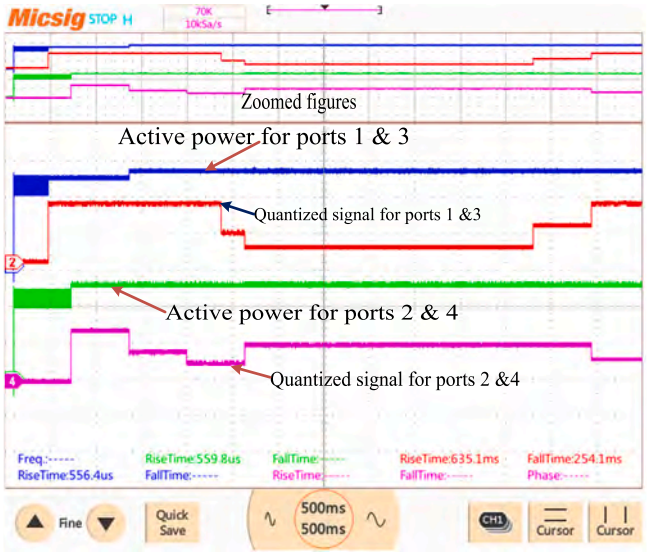


**Fig. 16.** Active power and quantified signals between ports.

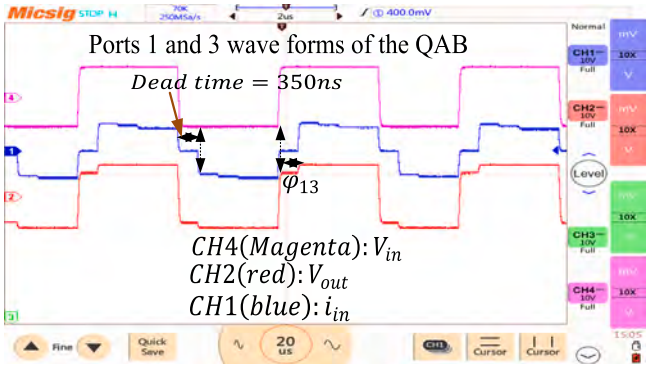


**Fig. 17.** QAB waveforms at Ports 1 and 3 under CMPC with ISMC.

Similarly, $P_{2\to4}$ increases from 1080 W to 1264 W at 0.01 s and reaches 1387 W after the PPL step at 2 s, remaining below the rated limit of 1500 W.

Figs. 20 and 21 present the SST waveforms with a 300 V input (scaled by 1/27) and a 48 V output voltage (scaled by 1/5). The system includes a 330 ns dead time between switching events, inter-bridge phase shifts ranging from 0.02 to 0.08 rad, and a measured delay of $29 \times 10^{-8}$ s between the ports.

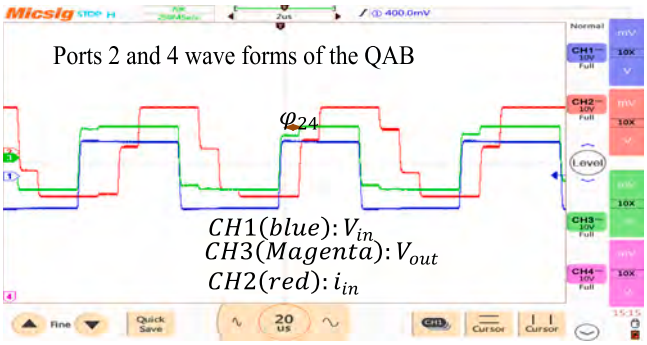


**Fig. 18.** QAB waveforms at ports 2 and 4 under CMPC with ISMC.

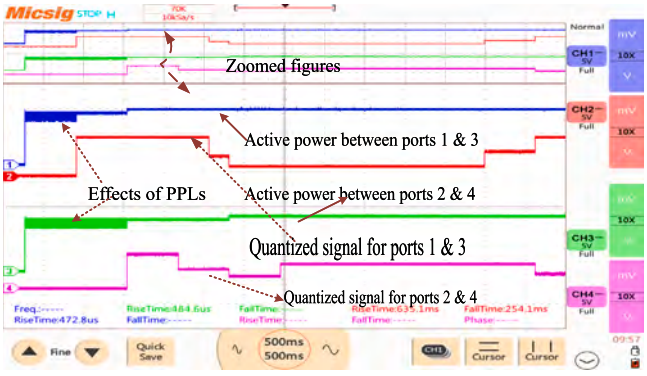


**Fig. 19.** Active power between ports and quantized signals for QAB.

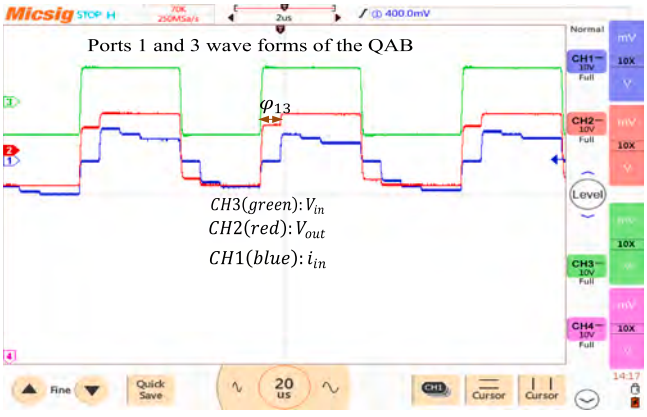


**Fig. 20.** QAB waveforms at ports 1 and 3 under IHOSMC.

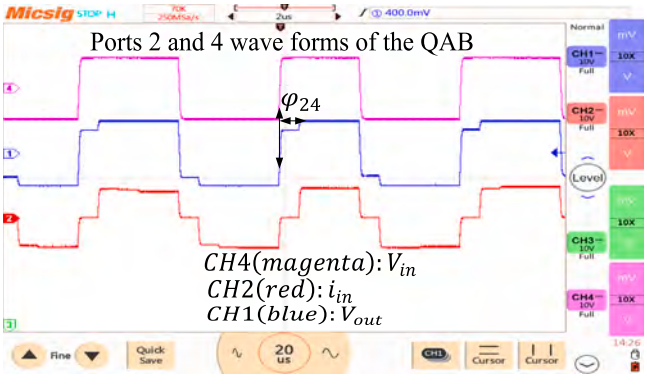


**Fig. 21.** QAB with IHOSMCQAB waveforms at ports 2 and 4 under IHOSMC.

## 5. Conclusion

This work developed an Adaptive Suboptimal Second-Order Sliding Mode Controller (ASSOSMC) and benchmarked it against the Integral Higher-Order Sliding Mode Controller (IHOSMC) and the Combined Model Predictive Control with Integral Sliding Mode Control (CMPC–ISMC) for a QAB resonant converter under pulsed power loads, validated using OPAL-RT hardware-in-the-loop (HIL). ASSOSMC provided the tightest voltage regulation ($\Delta V_3 = 0.5$ V, $\Delta V_4 = 0.3$ V) with a 3.6 µs settling time, but required higher current and exhibited preshoot that may increase thermal stress. IHOSMC achieved rapid convergence (6 µs rise time, 4.7 µs settling time) with low overshoot (0.667%), yet showed larger voltage dips (3.0 V at port 3 and 2.8 V at port 4) and currents of 2.5–2.6 A. CMPC–ISMC offered the best overall trade-off, maintaining low overshoot (0.667%) and fast settling (3.6 µs) while slightly reducing current stress ($I_3 = 2.4$ A, $I_4 = 2.5$ A) with smooth control action, making it the recommended option for stability-critical pulsed-load operation. Future work will integrate Artificial Neural Network (ANN) and Physics-Informed Neural Network (PINN) based adaptive estimation and online tuning to compensate pulsed-load disturbances and port coupling in real time, aiming to further reduce voltage deviation and current stress under uncertainties.

## CRediT authorship contribution statement

**Aphrodis Nduwamungu:** Writing – review & editing, Writing – original draft, Validation, Software, Resources, Methodology, Formal analysis, Conceptualization. **Tek Tjing Lie:** Writing – review & editing, Supervision, Resources. **Nirmal K.C. Nair:** Writing – review & editing, Supervision. **Ionis Lestas:** Supervision, Investigation.

## Declaration of competing interest

The authors declare the following financial interests/personal relationships which may be considered as potential competing interests: The authors declare that they have no known competing financial interests or personal relationships that could have appeared to influence the work reported in this paper.

## Acknowledgements

The authors would like to acknowledge the MBIE SSIF AETP project entitled ‘Architecture of the Future Low-Carbon, Resilient, Electrical Power System’ for financial support.

## References

[1] S. Ding, J. Wang, W.X. Zheng, Second-order sliding mode control for nonlinear uncertain systems bounded by positive functions, IEEE Trans. Ind. Electron. 62 (9) (2015) 5899–5909.
[2] T. Liu, X. Yang, W. Chen, Y. Li, Y. Xuan, L. Huang, X. Hao, Design and implementation of high efficiency control scheme of dual active bridge based 10 kV/1 MW solid state transformer for PV application, IEEE Trans. Power Electron. 34 (5) (2018) 4223–4238.
[3] Q. Sun, Q. Song, J. Meng, B. Cui, G. Li, F. Cheng, K. Wang, Flex-LCC: A new grid-forming HVDC rectifier for collecting large-scale renewable energy, IEEE Trans. Ind. Electron. 71 (8) (2023) 8808–8818.
[4] X. Guo, D. Zheng, F. Blaabjerg, Power electronic pulse generators for water treatment application: A review, IEEE Trans. Power Electron. 35 (10) (2020) 10285–10305.
[5] Q. Peng, Y. Yang, H. Wang, F. Blaabjerg, On power electronized power systems: Challenges and solutions, in: 2018 IEEE Industry Applications Society Annual Meeting, IAS, IEEE, 2018, pp. 1–9.
[6] M. Hosseinzadehtaher, A. Khan, M. Easley, M.B. Shadmand, P. Fajri, Self-healing predictive control of battery system in naval power system with pulsed power loads, IEEE Trans. Energy Convers. 36 (2) (2020) 1056–1069.
[7] L. Xu, J. Matas, B. Wei, Y. Yu, Y. Luo, J.C. Vasquez, J.M. Guerrero, Sliding mode control for pulsed load power supply converters in DC shipboard microgrids, Int. J. Electr. Power Energy Syst. 151 (2023) 109118.

[8] X. Dai, G.-P. Liu, W. Hu, Q. Deng, Consensus-based secondary control for DC microgrids with communication delays via a networked predictive control strategy, ISA Trans. 148 (2024) 387–396.
[9] M. Naderi, Y. Khayat, Q. Shafiee, F. Blaabjerg, H. Bevrani, Dynamic modeling, stability analysis and control of interconnected microgrids: A review, Appl. Energy 334 (2023) 120647.
[10] M.A. Hassan, C.-L. Su, J. Pou, G. Sulligoi, D. Almakhles, D. Bosich, J.M. Guerrero, DC shipboard microgrids with constant power loads: A review of advanced nonlinear control strategies and stabilization techniques, IEEE Trans. Smart Grid 13 (5) (2022) 3422–3438.
[11] P. Koohi, A.J. Watson, J.C. Clare, T.B. Soeiro, P.W. Wheeler, A survey on multi-active bridge DC-DC converters: Power flow decoupling techniques, applications, and challenges, Energies 16 (16) (2023) 5927.
[12] V. Sonnati, S. Arandhakar, K.P. Kumar, Soft-switching dual active bridge converter-based bidirectional on-board charger for electric vehicles under vehicle-to-grid and grid-to-vehicle control optimization, in: E3S Web of Conferences, Vol. 472, EDP Sciences, 2024, p. 01021.
[13] J. Cortés, V. Šviković, P. Alou, J.A. Oliver, J.A. Cobos, Comparison of the behavior of voltage mode, V 2 and V 2 I c control of a buck converter for a very fast and robust dynamic response, in: 2014 IEEE Applied Power Electronics Conference and Exposition-APEC 2014, IEEE, 2014, pp. 2888–2894.
[14] Z. Li, J. Chen, K. Li, Z. Xu, Y. Liu, M. Wang, Robust model predictive control for onboard interleaved multilevel boost DC-DC converter in DC shipboard microgrids, IEEE Trans. Transp. Electrification (2025).
[15] S. Paran, T. Vu, T. El Mezyani, C. Edrington, MPC-based power management in the shipboard power system, in: 2015 IEEE Electric Ship Technologies Symposium, ESTS, IEEE, 2015, pp. 14–18.
[16] D. Chavez, D.S. y Rosas, J. Tafur, Single-stage quad-active-bridge series-resonant AC-DC converter: Modulation for active and reactive power, in: 2023 IEEE Energy Conversion Congress and Exposition, ECCE, IEEE, 2023, pp. 2216–2221.
[17] Y. Xu, X. Ruan, X. Huang, Comparison of low pulse-repetitive-frequency pulsed power supplies with extremely small storage capacitor, IEEE Trans. Ind. Electron. 70 (11) (2022) 11194–11204.
[18] H. Jeong, M. Kwon, S. Choi, A high gain non-isolated soft-switching bidirectional DC-DC converter with PPS control, in: 2017 IEEE Energy Conversion Congress and Exposition, ECCE, IEEE, 2017, pp. 1723–1727.
[19] Z. Lin, W. Huang, R. Li, N. Tai, J. Liu, Adaptive damping ratio control of parallel buck converters for the marine pulsed power loads, IEEE Trans. Power Electron. 39 (9) (2024) 10989–11006.
[20] S. Bandyopadhyay, Z. Qin, P. Bauer, Decoupling control of multiactive bridge converters using linear active disturbance rejection, IEEE Trans. Ind. Electron. 68 (11) (2020) 10688–10698.
[21] Y.-M. Kwon, M.-W. Hwang, K.-C. Ko, Analysis and design of a pulsed power generator for a low-energy magnetic pulse welding system, Electronics 12 (24) (2023) 4921.
[22] M. Moradpour, P. Ghani, G. Gatto, A GaN-based battery energy storage system for residential application, in: 2019 International Conference on Clean Electrical Power, ICCEP, IEEE, 2019, pp. 427–432.
[23] L.F. Costa, G. Buticchi, M. Liserre, Quad-active-bridge DC–DC converter as cross-link for medium-voltage modular inverters, IEEE Trans. Ind. Appl. 53 (2) (2016) 1243–1253.
[24] J. Yan, J. Wang, Y. Chen, K. Huang, C. Shen, Large-signal model of pulsed power load for analysis of dynamic voltage and frequency, IET Gener. Transm. Distrib. 14 (12) (2020) 2271–2281.
[25] M. Bhardwaj, S. Yu, Bidirectional CLLLC resonant dual active bridge (DAB) reference design for HEV/EV onboard charger, Tex. Instruments (2020) 1–14.
[26] J. Han, X. Li, Y. Sun, S. Gong, S. Huang, Quadruple-active-bridge based unified power quality conditioner-L with fault current limiting capability, Electr. Power Syst. Res. 206 (2022) 107780.
[27] S.L. Mekonnen, G. Yang, B. Qu, Y. Peng, M.H. Patmal, P. Yang, Y. Xiao, Research on phase-shifted full-bridge ZVS DC-DC converter with multi-pulsed load, in: 2024 IEEE 10th International Power Electronics and Motion Control Conference, IPEMC2024-ECCE Asia, IEEE, 2024, pp. 4385–4390.
[28] W. Chen, K. Tai, M.W.S. Lau, A. Abdelhakim, R.R. Chan, A.K. Ådnanes, T. Tjahjowidodo, Robust real-time shipboard energy management system with improved adaptive model predictive control, IEEE Access 11 (2023) 110342–110360.
[29] A. Andre do Nascimento, Robust model predictive control for marine vessels, 2018.
[30] H. Yang, T. Li, Y. Long, Y. Xiao, Model-predictive-based power management for pulsed power load fed with multizonal shipboard power system, IEEE Trans. Transp. Electrification 10 (2) (2023) 4119–4128.
[31] F. Krismer, Modeling and Optimization of Bidirectional Dual Active Bridge DC-DC Converter Topologies (Ph.D. thesis), ETH Zurich, 2010.
[32] J.R. Rao, S. Venkateshwarlu, Soft-switching dual active bridge converter-based bidirectional on-board charger for electric vehicles under vehicle-to-grid and grid-to-vehicle control optimization, J. Eng. Appl. Sci. 71 (1) (2024) 49.
[33] A. Ahmed, N.K. Roy, A. Nasir, A novel weighted exponential sliding mode controller with a modified reaching law for the frequency regulation of a renewable integrated isolated AC microgrid, Electr. Power Syst. Res. 237 (2024) 111027.
[34] N. Vafamand, M.M. Mardani, M.H. Khooban, F. Blaabjerg, J. Boudjadar, Pulsed power load effect mitigation in DC shipboard microgrids: A constrained modelpredictive approach, IET Power Electron. 12 (9) (2019) 2155–2160.
[35] D.M. Raimondo, M. Rubagotti, C.N. Jones, L. Magni, A. Ferrara, M. Morari, Multirate sliding mode disturbance compensation for model predictive control, Internat. J. Robust Nonlinear Control 25 (16) (2015) 2984–3003.
[36] A. Ferrara, G.P. Incremona, M. Cucuzzella, Advanced and Optimization Based Sliding Mode Control: Theory and Applications, SIAM, 2019.
[37] M.M. Mardani, M.H. Khooban, A. Masoudian, T. Dragičević, Model predictive control of DC–DC converters to mitigate the effects of pulsed power loads in naval DC microgrids, IEEE Trans. Ind. Electron. 66 (7) (2018) 5676–5685.
[38] G. Bartolini, A. Ferrara, E. Usai, Chattering avoidance by second-order sliding mode control, IEEE Trans. Autom. Control 43 (2) (2002) 241–246.
[39] S. Laghrouche, F. Plestan, A. Glumineau, Higher order sliding mode control based on integral sliding mode, Automatica 43 (3) (2007) 531–537.
[40] G. Bartolini, A. Levant, A. Pisano, E. Usai, Higher-order sliding modes for the output-feedback control of nonlinear uncertain systems, in: Variable Structure Systems: Towards the 21st Century, Springer, 2002, pp. 83–108.
[41] A. Karbozov, M.G. Majumder, H.S. Krishnamoorthy, K. Rajashekara, Triple active bridge based multiport energy router for subsea–renewable interconnection, IEEE Trans. Ind. Appl. 59 (4) (2023) 4528–4538.
[42] L. Xu, J.M. Guerrero, A. Lashab, B. Wei, N. Bazmohammadi, J.C. Vasquez, A. Abusorrah, A review of DC shipboard microgrids—Part II: Control architectures, stability analysis, and protection schemes, IEEE Trans. Power Electron. 37 (4) (2021) 4105–4120.